Chapter 3

MOUNTAIN DEGRADATION MECHANISMS ON IO REVEALED BY GEOLOGIC MAPPING OF THE COCYCTUS MONTES REGION FROM JUNOCAM IMAGERY

C. H. Seeger[1], K. de Kleer[1], D. A. Williams[2], J. E. Perry[3], A. G. Davies[4], and D. M. Nelson[2]

"There's something ever egotistical in mountain-tops and towers, and all other grand and lofty things; look here,—three peaks as proud as Lucifer…This round gold is but the image of the rounder globe, which, like a magician's glass, to each and every man in turn but mirrors back his own mysterious self."

Moby Dick, Chapter 99: The Doubloon

Abstract

Periodic high-resolution documentation of Io is essential to understanding its surface evolution, from volcanic eruptions to tectonic motion to large scale mass wasting. *Juno* flybys of Io in 2023 and 2024 obtained imagery of the surface with the JunoCam imager at spatial resolutions comparable with those from the *Galileo* spacecraft (1996-2001). Areas of Io's north polar region were imaged for the first time, revealing high mountains in low phase angle observations. We are unable to identify detailed changes on mountain features due to the limited overlap and complementary nature of the high-resolution coverage between the *Galileo* and *Juno* datasets. However, the improved lighting conditions in the JunoCam imagery allow us to refine our understanding of previously mapped features,

[1]Division of Geological and Planetary Sciences, California Institute of Technology, Pasadena, CA 91125, USA.
[2]School of Earth and Space Exploration, Arizona State University, Tempe, AZ 85287, USA.
[3]Lunar and Planetary Laboratory, University of Arizona, 1541 East University Boulevard, Tucson, AZ 85721, USA.
[4]Jet Propulsion Laboratory, California Institute of Technology, 4800 Oak Grove Drive, Pasadena, CA 91109, USA.

including an extension of the rifting relationships previously proposed at Shamshu Patera. Cocytus Montes, a trio of mountains newly identified in the north polar region, exhibit several different geologic units grading from sharp features to eroded hummocks along their slopes. We present a geologic map of this region, and examine the interplay between the mountain units and the underlying layered plains which connect them on a raised plateau. Unique blocky deposits strewn across the plateau between these units have sparse analogs elsewhere on Io, and prompt questions about the erosional mechanisms acting on Io that may have emplaced them. We propose several formation mechanisms and conclude that some may be possible, but regolith creep-modified cliff collapse may be the most likely.

Plain Language Summary

Jupiter's innermost large moon Io is the most volcanically active body in the solar system, with a surface that is continually modified by eruptions (lava flows and gaseous plumes) and tectonics (fault motion and erosion via events like landslides). The Juno spacecraft made close approaches to Io in 2023 and 2024, obtaining images of the surface at high resolution and low sun angle--conditions which produce the long shadows necessary to see Io's topography. Though the new images do not overlap with the high-resolution images obtained 20 years prior by the Galileo spacecraft, they do capture parts of the north pole region in detail for the first time. We closely examined the northern region to create a geologic map, highlighting the different volcanic, mountain, and plains units visible here. We present several possible formation mechanisms for a newly defined geologic unit (a blocky deposit made of kilometer-scale chunks of crustal material), favoring a cliff-collapse mechanism above the others. We also identify several localities where sharper, less eroded mountain types gradually transition into slumped and eroded mountain types, capturing intermediate stages of erosion not typically visible on Io, with implications for the overall pace and process of erosion on a very active surface.

1. Introduction

Io is a world of constant, widespread volcanic activity (e.g., Davies, 2007). Io's volcanism is driven by an eccentric orbit forced by resonance with Europa and Ganymede (Peale et al., 1979). The resulting tidal stresses melt the interior enough to produce frequent and often voluminous volcanic eruptions, resurfacing the moon at a rate of ~ 0.1-1 cm year^{-1} (Carr et al., 1998; Geissler et al., 2004; Johnson et al., 1979). Basaltic to possibly ultramafic lavas, interlayered with sulfur-rich deposits and sulfur dioxide frost, are compressed continuously driving deep crustal subsidence stresses from crustal recycling (e.g., McEwen et al., 2004; McKinnon et al., 2001; Schenk & Bulmer 1998). These subsidence stresses may be relieved by intense faulting in all directions in the subsurface, uplifting large blocks of crust up to 16 kilometers high into towering mountains (Schenk et al., 2001). Io's crust is estimated to be 13-30 kilometers thick in order to support such large structures (Jaeger et al, 2003; Kirchoff & McKinnon, 2009; Schenk et al., 2001). Ionian mountains, while tectonic, differ from terrestrial mountains in that they are not long mountain ranges formed by plate movements, but rather form in tall, isolated massifs, usually elongate in nature, formed by subsidence stresses (Williams et al., 2011).

Io's extrusive volcanism (see summary in Davies, 2007 and Lopes et al., 2023) manifests as the emplacement of lava flows, both within paterae (caldera-like structures that are ubiquitous on Io) and on the extra-paterae plains, and as lava lakes in at least a few of the paterae. Gases exsolving from magma as it ascends, and released as a result of thermal interaction between lava flows and frozen sulfurous compounds on the surface, drive plume activity. The thermal emission from Io's volcanoes is so great that it is easily detectable from spacecraft and from telescopes on Earth (e.g., Davies et al., 2001; 2010; 2024; de Kleer et al., 2019; de Pater, et al., 2017; Lopes et al., 2001; McEwen et al., 1998; Perry et al., 2024; Veeder et al., 1994). The mechanisms for Io's volcanic eruptions are not entirely understood, but hypothesized models include magma, originating in the asthenosphere or from a magma ocean, feeding localized shallow magma chambers (Davies et al., 2006) and other crustal intrusions (Spencer et al., 2020). The magma then may exploit the tectonically fractured subsurface to rise along fault conduits (Jaeger et al., 2003; Keszthelyi et al., 2004).

Alternatively, hot spot-type magma ascension through crustal weaknesses in a heat-pipe regime (e.g., Kirchoff & McKinnon, 2009; McKinnon et al., 2001; O'Reilly & Davies, 1981) may feed volcanic eruptions. Analysis of *Galileo* and *Juno* data flyby show Io does not have a global magma ocean (Park et al., 2024), suggesting that a preponderance of magma originates in the asthenosphere.

Volcanic and tectonic forces work in tandem to both construct and destroy the iconic surface features distributed across Io's surface. Mountains, plateaus, and patera-bounding scarps all exhibit some form of degradation, likely triggered by a combination of gravity, volatile cycling, and volcanically-induced seismicity. These processes have previously been explored using imagery from the *Voyager* and *Galileo* spacecrafts, with *Galileo* providing high resolution (10s to 100s of meters/pixel) coverage of select regions (Keszthelyi et al., 2001; Turtle et al., 2004). Moore et al. (2001) detail the possible erosion mechanisms acting on scarps categorized in high-resolution *Galileo* imagery as belonging to four distinct classes: unmodified, alcoved, terraced, and containing basal debris cones. Scarp formation and modification or retreat could be attributed to liquid SO_2 sapping, plastic deformation and glacial flow of interstitial volatiles, sublimation-degradation, or disaggregation from chemical decomposition of solid S_2O (McCauley et al., 1979; Moore et al., 2001). However, the simplest and perhaps most universal mechanism is dry mass-wasting in the form of block release and brittle slope failure (Moore et al., 2001). Brittle failure on a much larger scale—10s of kilometers across—also likely modified the 10.5 km tall Euboea Montes, where large plates can be seen breaking with downslope movement in addition to more hummocky debris lobes (Schenk & Bulmer, 1998).

Previous studies have cataloged changes visible on Io's dynamic surface captured in the 17 years between the *Voyager* (1979) and *Galileo* (1995-2003) explorations of Io, and even over the course of each mission (Geissler et al., 1999, 2004; Keszthelyi et al., 2001; McEwen & Soderblom, 1983; McEwen et al., 1998; Turtle et al., 2004). In the intervening years, Earth-based telescopes and the *New Horizons* spacecraft (which performed an Io flyby in 2007) have provided additional evidence of active volcanism and, therefore, inferred surface modification (e.g., de Kleer et al., 2019a; de Pater et al., 2017; Rathburn et al., 2014). Now, 20 years after the *Galileo* mission concluded, the Juno spacecraft has obtained new high resolution images of Io with JunoCam, a "push-broom" visual-light imager, on two close flybys: PJ57 on December 30, 2023 and PJ58 on February 3, 2024. These images have a best resolution of 1.8 km/pixel (Ravine et al., 2024) and capture the north polar region of Io in unprecedented detail—including several mountains that were previously unidentifiable. The coverage of this new dataset is largely complementary to the highest resolution regions captured by *Galileo*, though there is some overlap in the PJ58 Jupitershine images; for example, the closely studied Hi'iaka Montes region appears along the limb in the Jupitershine image.

In this study, we use the higher resolution and favorable solar incidence angle (long shadows near the terminator are essential in distinguishing Io's topography) in the JunoCam dataset to provide a new perspective on previously mapped units, sharpening our understanding of mountains and paterae. We present several updates to the global database of surface features identifiable with this new perspective, and use the new imagery to expand on the sequence of rift events previously proposed for the Shamshu region. Finally, we present a regional geologic map of the northern mountains. These edifices, while morphologically consistent with their lower-latitude counterparts, exhibit a range of degradational styles and capture surface evolution in progress. We explore five possible formation mechanisms for a unique blocky deposit associate with these mountains, allowing us to expand on the possible erosional mechanisms modifying Io's surface features.

2 Methods

2.1 Global Relationships

All mapping and feature/imagery analysis was based on previous mapping efforts; namely, the USGS Geologic Map of Io based on mosaiced global imagery from the *Galileo* and *Voyager* spacecraft flybys (Williams et al., 2011). This map contains shapefiles denoting the geologic units mappable at the global 1 km/pixel resolution, including paterae, mountains, and plains (subdivided into several morphotypes). Using ESRI ArcGIS Pro™ software, a new mosaicked basemap of Io using imagery from the PJ57 and PJ58 JunoCam flybys was projected into the same simple cylindrical coordinate plane for direct comparison between the new and old data. Variable lighting conditions between the new JunoCam images taken at different times of day from *Galileo* and *Voyager* images, along with differences in resolution of the coverage, give us new perspective on the surface features—namely, mountains and paterae—that have been previously mapped. A low incidence angle is often required to distinguish topographic relief in Io's mountains (e.g., Schenk et al., 2001; Turtle et al., 2001; Jaeger et al., 2003).

A systematic, side-by-side comparison was performed for all identifiable mountains visible in JunoCam imagery between the new and prior basemap. The focus of this mapping comparison was to identify surface features that may have changed (e.g., mass wasting deposits, changes in shape to paterae, newly uplifted scarps, etc.), or to note features that remained the same throughout the 20-year time gap in the imagery. Because the JunoCam PJ57 imagery has a maximum resolution of 1.84 km/pixel, detectable changes were limited to large-scale changes to overall feature shape; textural evolution of individual slopes, while likely over this time interval, is beyond the limitation of this dataset. However, the new perspectives on several previously-mapped surface features with updated resolution and lighting conditions allowed us to suggest several updates to the database of previously mapped features, where a mapped patera now clearly stands up in positive relief, or the shape of a mountain is better defined (Figure 1).

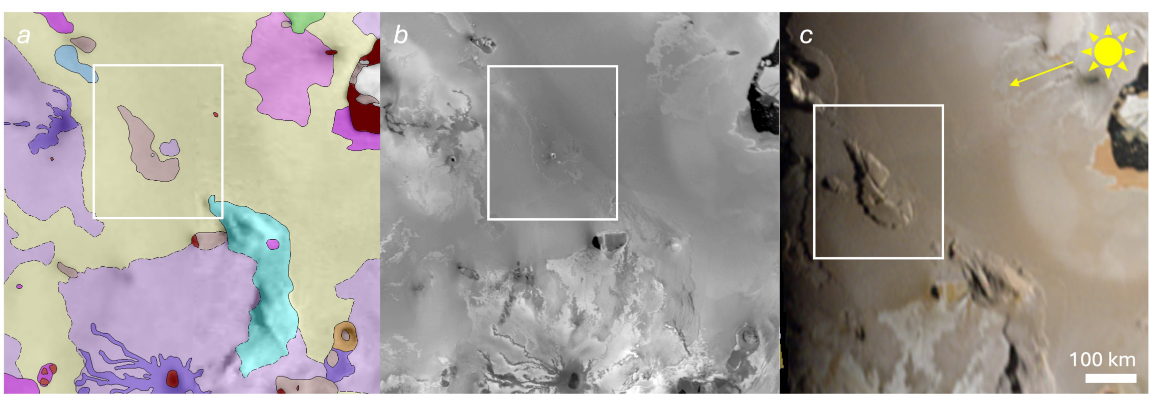

Figure 1. Near-terminator illumination conditions provide new perspective on a feature adjacent to Loki Patera that was originally mapped as a patera in (a) the USGS Geologic Map of Io (Williams et al., 2011) using (b) high sun angle imagery from *Galileo* and *Voyager*, but is evident as a topographic high and should be reclassified as a mountain

based on (c) JunoCam PJ57 coverage of this same area. Images are centered at 6° N, 36° E; north is up .

2.1 Northern Regional Map

The JunoCam imagery provides new images of the previously unresolved north pole region of Io, from 55˚ latitude northward. Previous features were inferred from *Galileo* and *Voyager* coverage, but new polar mountains and paterae can now be mapped for the first time (Williams et al., 2024). Using ArcGIS Pro™ and a basemap with an orthographic projection centered at 60N 330W to minimize distortion, we created a regional map at 1:500,000 scale of the new mountainous region of interest for this study, using geologic units and symbology consistent with those presented in Williams et al. (2011) as well as previous local geologic mapping efforts of a comparable scale (Bunte et al., 2008, 2010; Leone et al., 2009; Williams et al., 2002, 2004, 2005, 2007). Units are defined and classified based on morphology, albedo, and color, and depositional, erosional, and evolutionary sequence is inferred based on superposition and cross-cutting relationships between units.

One of the most distinguishing features in the northern region is the large scattered blocks of rock distributed across the layered plains between the northwestern and northeastern mountains. Using the orthographic projection centered among these mountains, ArcPro was used to measure the size of the blocks (as best as they can be distinguished from shadow, at just a few pixels wide) and distance from the top of the nearest peak (as best as could be distinguished, as the mountain summit falls along the terminator). The USGS's Integrated Software for Imagers and Spectrometers (ISIS; Rodriguez, 2024) qview program was used with the EDR dataset to measure block height (as well as scarp heights) using processed individual .cub frames derived from a JunoCam processing pipeline (Perry et al., 2024, following Perry et al., 2022). The Red filter observation was favored due to its higher signal-to-noise than the Green and Blue bands. Measurements were made using the red filter individual framelet (JNCE_2023364_57C00022_V01_RED_0013) to calculate the size of each shadow thrown from the blocks. These measurements were combined with solar incidence angle to calculate block height using Equation 1, with a 1 pixel error on line length measurements.

Shadow Geometry Equation *(1)*

$$\text{Height} = \text{Shadow Length} * \tan(180 - \text{Sun Azimuth in degrees})$$

3 Results

3.1 Insights from Junocam Imagery

3.1.1 Search for Temporal Changes in Io's Surface

Direct side-by-side comparisons of the same geographical regions covered by *Voyager*, *Galileo*, and new JunoCam imagery taken under different solar incidence angle conditions illuminate changes and consistencies in Io's topography over the approximately 45-year time interval spanned by these datasets. Io is a dynamic body with frequent volcanic eruptions and evidence of erosional processes such as mass wasting and scarp retreat via sapping (e.g., Moore et al., 2001). Therefore, identifying surface changes such as large-scale mountain shape alteration due to mass wasting would place constraints on the erosion rates degrading Io's tall topography. In all surveyed mountains (due to JunoCam imagery covering ~50% of the global *Galileo*/*Voyager* coverage), there were no discernable changes in shape and no identifiable debris fans or changes in scarp sharpness from the twenty-year-old dataset to today's. Even mountains proximal to active, erupting paterae remained unchanged in appearance at the JunoCam pixel scale of 1.8 km. We also do not see any evidence of tectonic motion indicative of reactivation (extension) along compression fault lines. That is not to say surface modification did not occur—it is extremely likely that many steep mountain slopes have new landslides, textural changes, and debris fans—but any such evidence would require data with a higher spatial resolution.

A few regions exhibit putative changes at the limit of image resolution. These are presented in Supplementary Figure 1. Future higher resolution imagery of these regions could confirm the extent of alteration and place constraints on rates of erosional processes.

3.1.2 Feature Reclassification

JunoCam imagery provides new perspectives on several previously-mapped and classified mountains and paterae due to improved resolution and solar incidence angle. We provide a catalog of locations where the new view on published USGS geologic units (Williams et al., 2011) calls for a reclassification of features (Table 1; Supplementary Figure 2). Dominantly, we suggest updates to mountain extent and mapped paterae that are now discernable as positive relief mountain features. While there are 10 features that were identified for reclassification based on a global survey, these updates could be significant in future studies that survey the number and location of tectonic and volcanic features, as well as their shapes and relationships to each other.

Table 1. Reclassified geologic units based on JunoCam imagery. Object ID corresponds to published Geologic Units in USGS Geologic ArcGIS map file (Williams et al., 2011). Longitudes are given in 0-180° format, East positive. Corresponding images are given in Supplementary Figure 2.

Object ID	Latitude	Longitude	Name	Previous Classification	New Classification	Rationale
879	8.52	33.31		Patera floor, undivided	Mountain	Better lighting shows positive relief
941	15.13	27.85		Bright plains	Layered Plains	Better lighting shows previously unmapped layered plains unit
1415	57.50	106.60	Nile Montes	Mountain, lineated	Mountain, lineated	New perspective on shape
1365	50.20	110.80	Nile Montes	Flows, dark; Flows, undivided	Mountain, lineated	Flows reinterpreted as slumping mountain material
1420	59.20	164.00		Flows, undivided	Layered Plains	Flows reinterpreted as lower layered plain component of pleateau mountain
1345	47.00	162.00		Flows, bright	Mountain, undivided	Better lighting highlights scarps, better defining mountain
1380	53.61	161.93		Patera floor, undivided	Mountain, undivided	Better lighting shows positive relief
213	46.85	10.36		Flows, undivided; Red-brown plains	Patera floor, dark; Patera floor, undivided	New imagery reveals unmapped patera
695	-8.0949	114.5406	Pillan Mons	Patera floor, undivided	Layered Plains	Better lighting shows positive relief
438	-26.271	16.18887		Red-brown plains; Bright plains	Layered Plains	Layered plains continue to edge of patera; uplift potentially post-dates lava flow

3.1.3 A More Detailed Look at the Shamshu Region

Previous studies have examined closely the region surrounding Shamshu Mons (Bunte et al., 2010). West Shamshu Mons and Shamshu Patera are covered in 340–345 m/pixel detail in one *Galileo* SSI observation obtained during the orbit I27 flyby (I27ISSHMSHU01; PIA02555), along with small corners of what Bunte et al. (2010) have informally classified as North and South Shamshu Montes, which are otherwise barely discernable in the low-resolution *Galileo* coverage (Figure 2). The JunoCam PJ58 flyby coverage of this same region in 1.01 km/pixel detail using Jupitershine illumination provides a new, complete view of these two mountains in unprecedented detail. The overall structure of South Shamshu Mons is a lineated mountain with mottled material to the west, and an adjacent connected lobe to the east. This adjacent lobe lacks discernable features in the JunoCam imagery, but has two scarps illuminated in the *Galileo* imagery that led to its previous classification as its own independent undivided mountain. The Shamshu region is located ~370 km east of the distinctive Hi'iaka Montes region (measured From Hi'iaka Patera to Shamshu Patera), where two large, L-shaped mountains are interpreted to have been rifted apart by translational and extensional tectonics (Bunte et al., 2010; Jaeger et al., 2003). Based on the available *Galileo* data at the time, Bunte et al. (2010) propose a similar regime for the Shamshu region.

The updated view of North and South Shamshu Montes provided by JunoCam allows us to develop this model. Both North and South Shamshu Montes are large edifices (over 150 km across) with multiple morphologies expressed, but distinct parallel ridges at the ends closest to Shamshu Patera. The similarities between these ridges support the interpretation that these edifices could have once been joined, formed by an earlier compressive uplift episode, with the new larger view of the extent of the ridges leading us to suggest a slight modification to the Bunte et al. (2010) reconstruction (Figure 3). A NE/SW oriented right lateral strike-slip fault with an accommodating extensional rift where Shamshu Patera opens could easily restore North and South Shamshu Montes to one morphologically consistent edifice. A perpendicular extensional rift at the location of Shamshu Patera would provide accommodation space for lava buildup from successive eruptions, with the darkest, freshest lava concentrated at the NE end of the patera, adjacent to the eroding scarp of North Shamshu Mons, where the rift would be opening. Though Shamshu Patera cuts into the flank of North

Shamshu Mons, the lack of debris on the patera floor in the *Galileo* imagery suggests that later-stage volcanic resurfacing could have obscured fallen debris from mountain degradation (Bunte et al., 2010; Turtle et al., 2001). JunoCam imagery similarly does not contain any resolvable debris cones or major scarp retreat, indicating this to be a stable process over the twenty-year gap between datasets—unsurprising for such a short interval in geologic time. West Shamshu Mons could also have been part of a singular mountain complex; though it is not morphologically consistent with the parallel ridges of North and South Shamshu Montes, it does have demonstrate some similarities in orientation to the eastern lobe of South Shamshu Mons, indicating that they both could have been formed by similar uplift regimes. However, West Shamshu Mons sits 80 km west of Shamshu Patera, and there is no resolvable evidence for long-term rifting transporting it westward; older lava flows associated with this rifting could have degraded beyond recognition at the current resolution, or West Shamshu Mons formed independently from the North-South Shamshu complex.

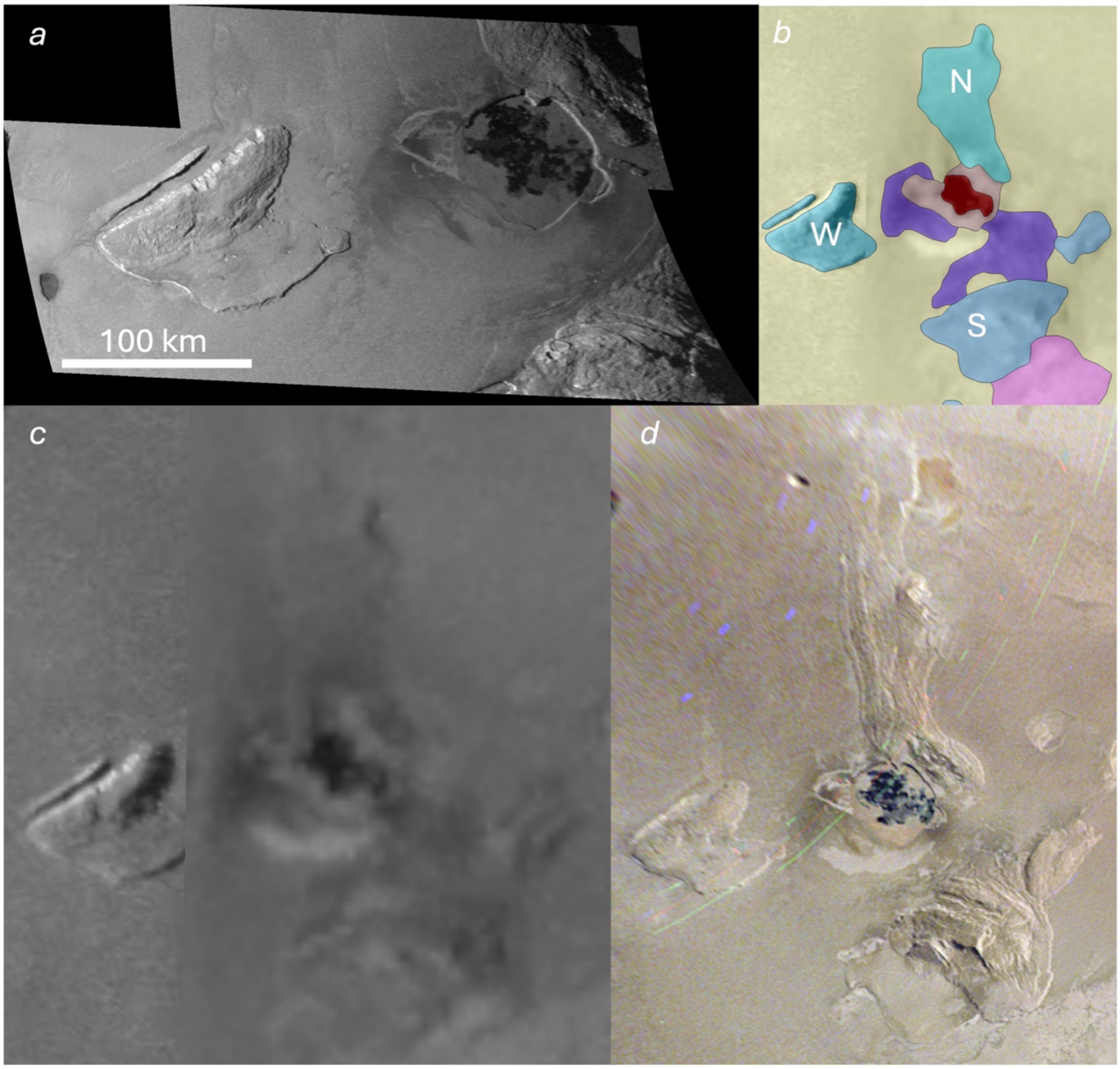

Figure 2. Image coverage and interpretations of Shamshu region of Io, including Shamshu Montes and Shamshu Patera. (a) *Galileo* high resolution image (I27ISSHMSHU01, 340-345 m/pixel), with image centered at 11° S, 68° W; (b) global geologic map of the three mountain units and Shamshu Patera (Williams et al., 2011); (c) *Galileo* low resolution coverage (frames 5 and 6 in global USGS map, corresponding to observation/image numbers C9ISSRFMON01/ 0401785378 and C10ISIOTOPO02/ 0413659700); (d) JunoCam PJ58 Jupitershine image (JNCE_2024034_58C00024_V01) capturing the mountains north and south of Shamshu Patera for the first time in their entirety.

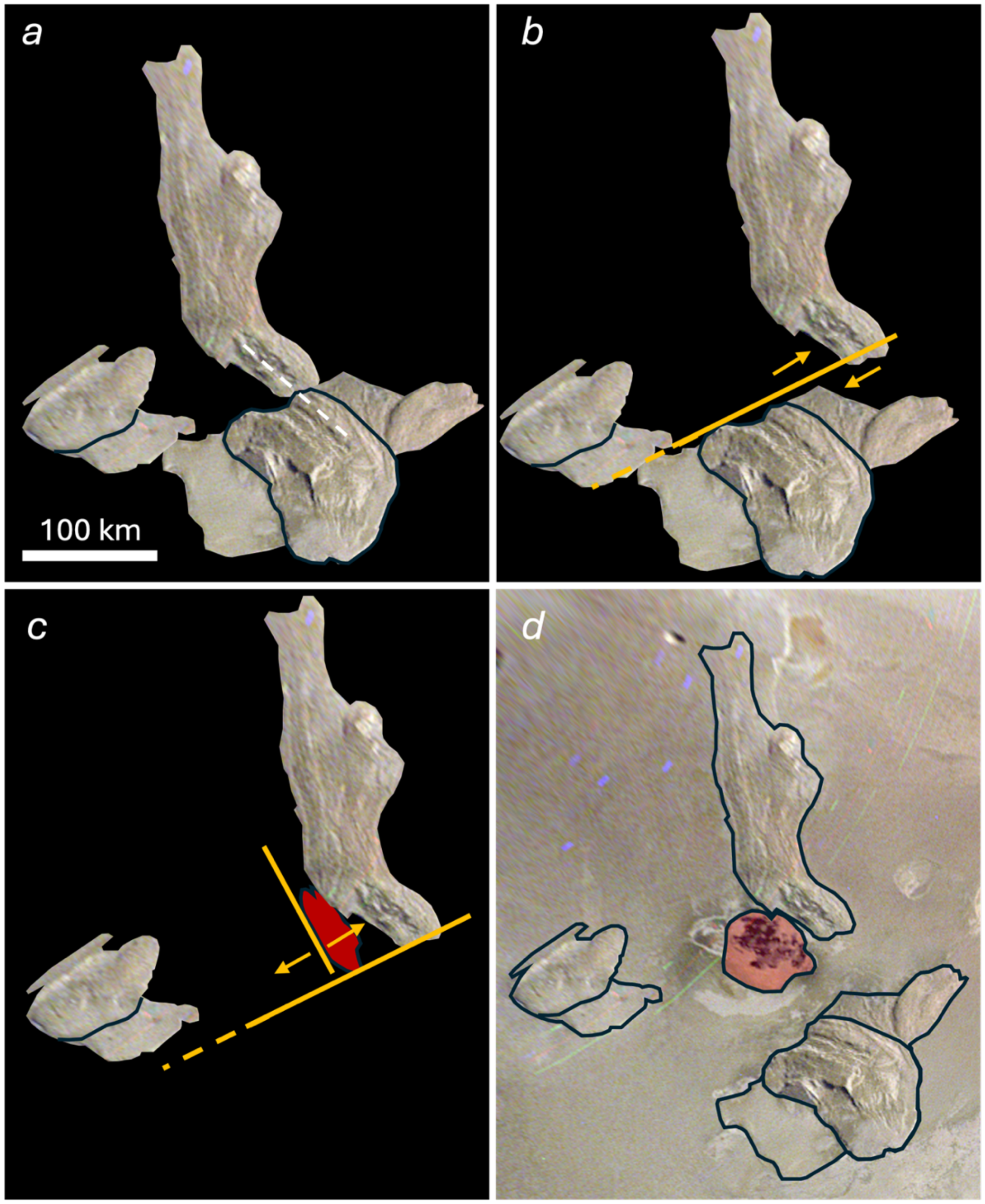

Figure 3. Reconstruction of possible tectonic history in Shamshu region, modified after Bunte et al. (2010) Figure 12. (a) North and South Shamshu Montes are initially one related edifice with aligned linear ridges (dashed white line) while the morphologically similar layered plains on West and South Shamshu Montes are continuous; (b) Right lateral rifting initiates, separating North and South Shamshu Mons; (c) initiation of the Shamshu Patera formation via a rift to accommodate the strike-slip motion of the primary fault while continued extension further separates the mountains; (d) current configuration, with Shamshu Patera siting between the three mountain units.

3.2 Geologic Map of Cocytus Montes

JunoCam coverage during PJ57 provided novel views of Io's northern polar region, including several mountains imaged at 1.84 km/pixel. The low solar incidence angle—approximately 10 degrees, adjacent to the terminator—highlights the topography in sharp relief. We use this new imagery to map five broad geologic units, following conventions employed in the previous suite of regional geologic maps produced from *Galileo* data (Bunte et al., 2008, 2010; Leone et al., 2009; Williams et al., 2002, 2004, 2005, 2007): mountain materials (including plateaus), plains materials, volcanic materials (including paterae and lava flows), bright diffuse deposits, and a newly-defined unit of blocky material. Symbology for units, structural features, and contacts follows the symbology presented in the USGS global geologic map of Io, and we refer the reader Williams et al. (2011) for detailed unit descriptions and interpretations. Here, we highlight the relevant units as summarized in Table 2, along with their interpreted relationships to each other as derived from the regional geologic map (Figure 4).

The northern mountains express the same morphologies as their more equatorial counterparts, with a mix of lineated and mottled units (Williams et al., 2024; Ravine et al., 2024). The area of focus for this regional geologic map is defined by a three-mountain system, Cocytus Montes, with three tall (several km) peaks connected by a system of apron-like layered plains, some of which are uplifted as 1-3 km tall plateaus. The morphology of lineated mountains adjacent to plateau-like layered plains is similar to mountains like West Shamshu Mons, Gish Bar Mons, and several others. However, a new geologic unit of blocky material—composed of kilometer-scale blocks scattered across the layered plains adjacent to the northwestern mountain—has been identified as a unique deposit type not previously recognized on Io. We explore possible formation mechanisms for these blocks in Section 4.1. In addition, scarps along plateau margins, and the blocky region in particular, are closely associated with halo-shaped white diffuse deposits interpreted to be SO_2 sapping at retreating scarps (Moore et al., 2001).

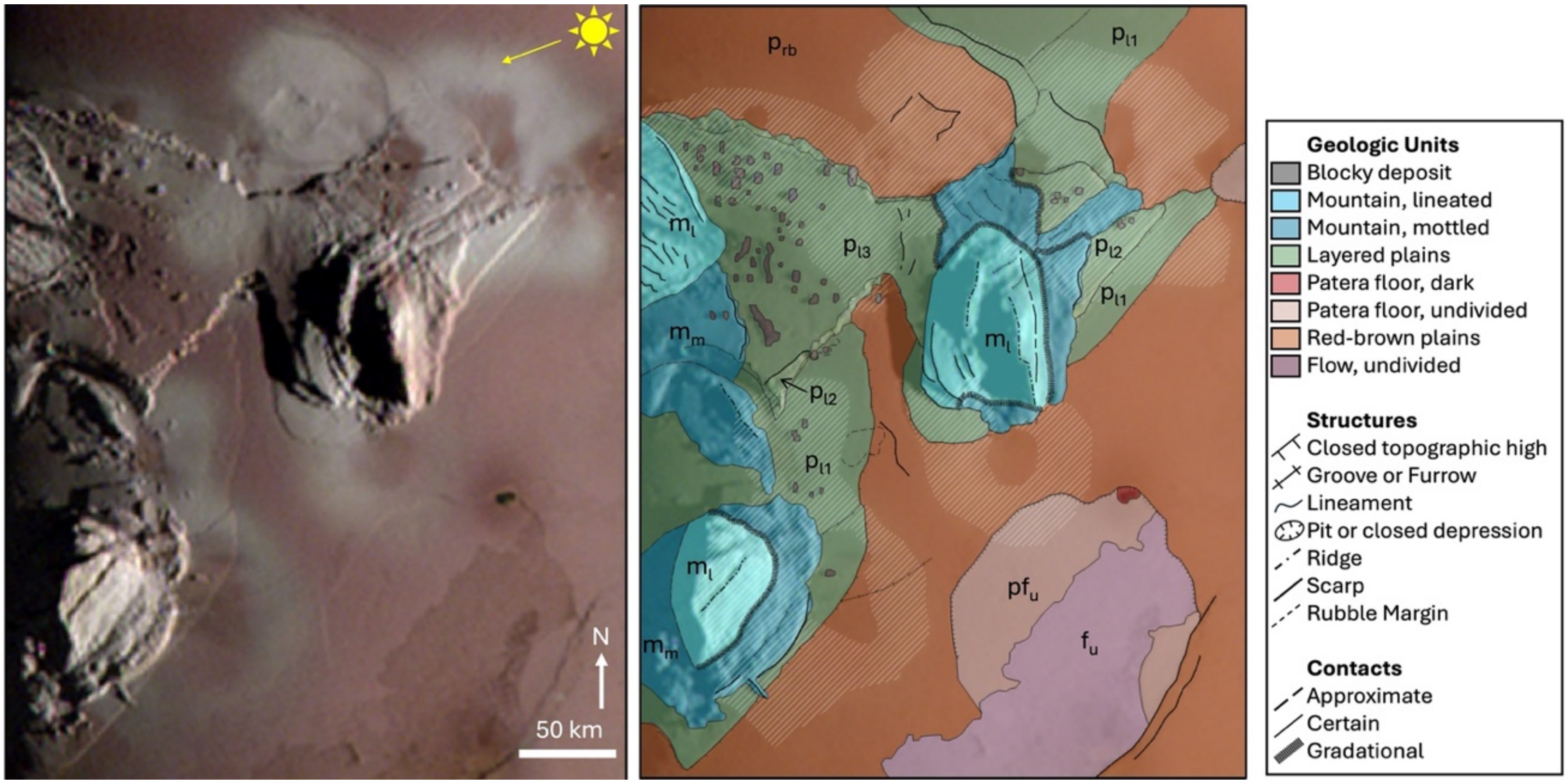

Figure 4. Regional geologic map of Cocytus Montes (composed of West, East, and South Cocytus Mons) using orthographic projection centered on 60N 330W (left). Geologic units (right) are consistent with global geologic units presented in Williams et al. (2011), with an additional blocky deposit unit newly identified and defined here. The reader is referred to full unit descriptions in Table 2 for unit abbreviations shown on map. Map covers 52.3-66.6° N, 11.2-39.2° W.

Table 2. Geologic units identified in northern regional geologic map.

Material Units	Description	Interpretation
Lineated mountain material (ml)	Contains the sharpest scarps, deep shadows cast by prominent ridges, and relatively smooth and sheer faces. Can contain many blocks of uplifted, subparallel plate-type material, and sometimes exhibit lineations on the steep, sheer faces.	Uplifted crustal blocks exhibiting minimial degradation or erosion by downslope slumping or mass wasting. Parallel lineations on the northwestern mountain face may indicate some slumping, although they are not quite parallel to the scarp boundary at the lineated mountain/layered plains contact; similar lineated textures observed on other mountains generally form perpendicular to the slope.
Mottled mountain material (mm)	Characterized by domical mounds of material with few scarps and ill-defined lineations. This unit does contain isolated grooves or furrows, and lobes of material extend out upon underlying plains material.	Material displaced by gravity in a downslope direction, by mechanisms such as mass wasting with or without rotational sliding.
Red-brown plains material (prb)	The interstitial material blanketing the surface between the topographically distinct tectonic and volcanic features.	While Io's surface boasts three colorful plains units on a global scale (yellow, white, and red-brown; Williams et al., 2011), the only morphology present in this mapping area is red-brown, interpreted to be the product of alteration of surficial frosty sulfur compounds by radiation exposure (Johnson, 1997; Geissler et al., 1999).
Layered plains material (pl)	Isolated regions of relatively smooth plains material that are separated from the underlying plains (and each other) by distinct bounding scarps. Several layers are defined (pl1-3), creating large, apron-like plateaus surrounding and even connecting the northeast and northwest mountains.	Silicate crust mantled by sulfur-rich materials exposed on local topographic highs with boundaries defined by degradational processes.
Blocky deposit	Isolated ~2-10 kilometer-wide massifs identifiable by slight albedo/color differences from the underlying plains and measurable shadows. Largest population sits atop a plateau, though several blocks are measured directly adjacent to plateau-bounding scarps.	Blocks of silicate crust originating from mountains or layered plains and deposited by erosional mechanisms across and adjacent to layered plains units.
Diffuse deposit	White material that occurs in characteristic circular to irregular patches, most often along scarp edges, that lightly mantles all underlying units including red-brown plains, layered plains, and mottled and lineated mountainsides.	Volcanic deposits consisting of dust and condensed sulfur dioxide gas (Carlson et al., 1997).
Dark patera floor material (pfd)	Dark material that is uniformly black in color at the image resolution, round in shape and filling topographic depressions, and is aligned at the edge of the curved patera-bounding scarp separating this feature from the red-brown plains.	Warm, recently-emplaced silicate flows or crusted lava lakes (Lopes et al., 2001; Davies et al., 2001; Radebaugh et al., 2001, 2004).
Undivided patera floor material (pfu)	Neither bright nor dark in color or albedo, and is only separated from the plains by the patera-bounding scarp. Mapped unit is overlain by undivided flow.	Crusted and cooled lava flow or lava lake, older than dark patera floor material.
Undivided flows (fu)	Intermediate relative albedo and limited texture at the map resolution. Bounded on the east by scarps, and continues to the south potentially beyond the patera walls.	Lava flows of indetermninate composition, though likely mafic flows originating from patera but mantled by sulfur-rich materials.

3.2.1 Mountain units: gradational contacts linking mountain morphologies

The mapped mountain units are subdivided into lineated mountains, mottled mountains, and layered plains, with several tall (3-5 km lower limit, based on shadow measurements) isolated peaks extending above the surrounding plains, separated by well-defined bounding scarps. While gradational contacts have been identified between mountain units and layered plains elsewhere on Io, this mapped region contains gradational contacts between lineated mountains and mottled mountain material as well. Lineated mountains are interpreted to be the most pristine mountain type, formed tectonically by faulting, uplift, and the subsequent collapse of tall edifices (Schenk and Bulmer, 1998; Turtle et al., 2001, 2004). Mottled mountains are interpreted to be the degraded counterparts of lineated mountains that have undergone mass-wasting processes (Turtle et al., 2001). Previous coarser scale studies (e.g. Crown et al., 1992; Williams et al., 2011), characterize the mountains as being one of these two mountain types. However, we determine two of the three mountains in our study area to capture an intermediary stage of degradation: the uppermost flanks of the mountain retain the sharp scarps of lineated mountains, but there are several areas where hummocky material related to slope failure appears to extend downslope onto the layered plains and bright plains below.

3.2.2 Layered plains: identification of blocky deposits

While some of the lowest-lying plateau-like layered plains units (p_{l1}) do not stand tall above the surrounding plains, the unit that extends between the lineated mountains (p_{l3}) is characterized by tall, sharp bounding scarps, possibly scalloped in places, with some adjacent large blocks and smaller scale rubble piles. Cliff tops are mapped as closed topographic highs, while geologic unit boundaries include the furthest extent of rubble extending below the scarp top. The western portion of this plateau also contains the majority of the scattered blocks (see Section 3.2.3 Blocky Deposits). Shadow measurements from the eastern portion indicate a gently sloping (~3% grade) surface, from 2.93 +/- 0.23 km down to 1.57 +/- 0.29 km over a span of 50 km. A subtle furrowed texture including some mapped lineations across this surface could be a potential expression of downslope creeping processes akin to terrestrial soil ripples or lunar “elephant hide” texture, though on the kilometer scale rather than centimeter to decameter scale on Earth or the Moon (Anderson & Anderson, 2010;

Highland & Bobrowsky, 2008; Lindsay, 1976; Melosh, 2010). While illumination conditions do not permit equal quality measurements of the western portion of this unit, a minimum height estimate of 3.32 +/- 0.3 km indicates that this portion slopes eastward to meet the layered plains of the northeast mountain.

Layered plains have been interpreted to be the result of tectonic activity and/or downslope slumping and mass wasting, possibly from adjacent mountains, with scarps modified by slumping or SO_2 sapping, among other processes (e.g., Moore et al., 2001; Turtle et al., 2001). In the case of similar morphologies to the mapped mountains, such as West Shamshu Mons, the analogous plateau portion of the mountain may have formed from large-scale gravitational sliding of a detached upper layer, composed of lava flows, that was not cohesive with the full tilted crustal block during uplift (Bunte et al., 2010), as opposed to a large-scale mass-wasting formation (*sensu* Schenk and Bulmer, 1998). Our mapped layered plains' relationship to the blocky deposits adjacent to scarp edges may also indicate a large-scale rotational cliff failure erosional mechanism, as explored in Section 4.1.

3.2.3 Blocky Deposits: a key to erosional processes

There are 58 blocks identifiable in the study region, and 41 of these are distributed across the two layered plains unit (p_{l3}) adjacent to the northwest mountain (Figure 4). The remaining smaller populations of blocks are distributed across layered plains adjacent to the other two mountains, and several blocks are identified at the lower boundary of the layered plains, at the base of the scarp. Blocks are considered measurable if they are greater than two pixels across, there is a distinct color or albedo difference to differentiate them from the surrounding plains, and they cast a measurable shadow; JunoCam imagery covers these blocks very close to the terminator, providing the necessary illumination conditions to see these unique features. It should be noted that there are likely blocks smaller than is resolvable, and the angularity and distribution of the blocks may be affected by the pixel scale. Block heights measured from shadow lengths (Equation 1) indicate that these blocks are wider than they are tall by a ratio of ~6.5:1 on average. That is, they are shaped more like thick slabs than cubes, with diameters of several kilometers. These block dimensions may have implications for formation of this unit, as explored in Section 4. Their distribution across the plateau is irregular, and there are no correlations between block size and distance from the adjacent mountain summit (inferred to be along the terminator), though the largest blocks, which are elongate features somewhat parallel to the adjacent scarp boundaries, are closer to said respective scarps (Figure 5).

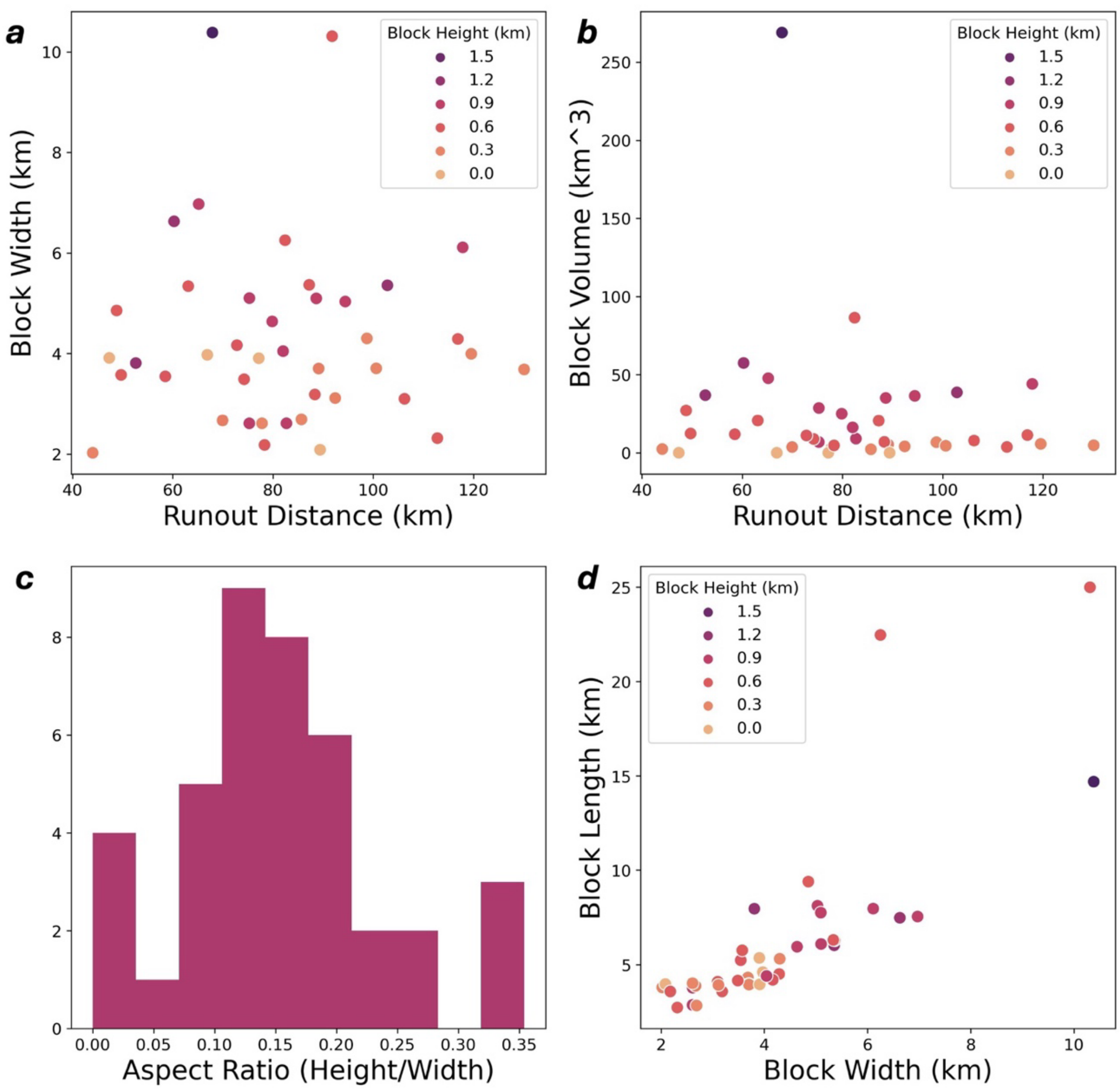

Figure 5. Size and distance parameters for 41 measured blocks on plateau in mapped area. Dataset includes the three long, more sinuous blocks mapped on p_{l3}, which correspond to the three largest data points. Block width and length are geodesic measurements of the planform long and short axes. (a) Block size vs. runout distance from the nearest measurable mountain "summit," measured with block width representing the intermediate

axis; (b) block size vs. runout distance, measured with calculated volume; (c) distribution of aspect ratios for all measured blocks using width as intermediate axis; (d) a linear relationship between block width and block length. Block height measurements have an error of 1 pixel, corresponding to 0.25 km.

The northern blocky deposit is a new feature type, now identifiable because of the resolution and low sun angle captured by JunoCam. Similar mountain-adjacent layered plains were inspected for similar features, and several potential isolated blocks were detected on the flanks of West Shamshu Mons; these blocks were not previously identified in close regional studies of the Shamshu region (e.g., Bunte et al., 2010), but we are now able to locate them by using the northern blocky deposit as a reference (Figure 6a). This example serves as the closest analog to the blocky deposit, because the two groups of blocks (yellow circle and black arrows) lie atop their respective plateaus of layered plains (which are interpreted to be an erosional deposit from the adjacent mottled mountain material), just as the Cocytus Montes blocks do. There are also several instances of layered plains apparently degrading into large blocks, both in the northern region and across Io (Figure 6b-g). It is not currently clear if the layered plains degradation blocks are formed by the same processes as the plateau-topping blocks, as discussed in Section 4, but they are included for completeness. These secondary examples all occur at the scarp boundary where layered plains or mottled material transitions to basal plains.

Interestingly, all of these alternate block locations are devoid of the halos of white diffuse deposits so common in the northern map region. Some of the plateau-topping blocks sit within a white diffuse halo zone, while some do not. Some of the scarp-adjacent blocks sit within white diffuse halos, while some do not (Figure 4). It is possible the release of SO2 gas from scarp walls, if that is indeed the source of the white diffuse deposits, could contribute to scarp failure in the form of large blocky debris, but these results are inconclusive.

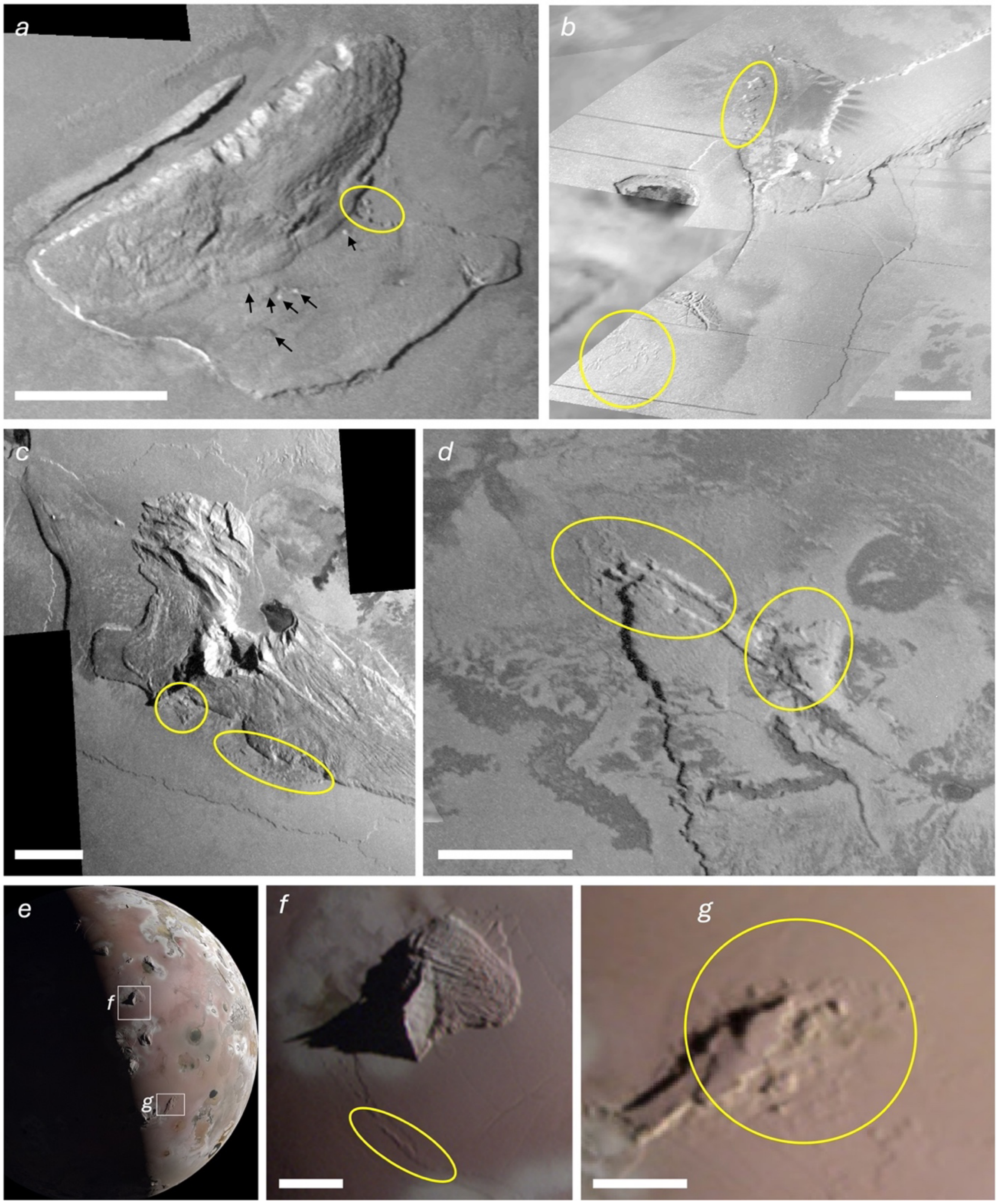

Figure 6. Detections of large blocky debris adjacent to mountains on Io and sitting atop layered plains or red-brown plains. Images captured by *Galileo* (a-d) and JunoCam PJ57 (e-g). Scale bar in all images is 50 km. Image centers are located at: (a) 11° S, 72° W; (b) 37° N, 84° W; (c) 28° S, 161° W; (d) 31° N, 162° W; (f) 43° N, 37° E; (g) 69° N, 37° E.

3.2.4 Diffuse deposits: constraints on scarp retreat

Elsewhere on Io, white diffuse deposits are interpreted to be the products of vaporization, condensation, and reaccumulation of SO_2 (and contaminants) around flow margins (Kieffer et al., 2000; Milazzo et al., 2001). The white diffuse deposits association with scarps—particularly bounding layered plains—and the lack of proximal vents or flows indicates these deposits might rather be the result of seepage from fractures (McCauley et al., 1979). Their relationship to the underlying units is not entirely clear in this locality. Diffuse deposits of the other colors visible on Io (Williams et al., 2011) are not present in the mapped region.

Across Io, diffuse deposits are ephemeral features that easily evolve or become overprinted (Carlson et al., 1997; Douté et al., 2001; Geissler et al, 1999). While cataloging the changes to diffuse deposits between the *Galileo*/*Voyager* and JunoCam datasets is outside the scope of this surface feature-focused study, we do note consistencies in the similarly scarp-adjacent white diffuse deposits in the Euboea Fluctus region (outside the regional map extent), suggesting that these jets are sustained over the 44 year time interval without producing measurable scarp retreat (Figure 7). Pixel sizes in this region are 848 m/pixel, and scarp retreat would need to occur over several pixels to cause a detectable change in the surface expression of the shape of the scarp. Therefore, we can place a bound on the rate of this erosional mechanism, where scarp retreat is happening slower than ~200 m/year. While this is an unreasonably fast rate on geologic timescales, it is nonetheless a useful constraint for erosional models on a highly active surface provided by the given datasets.

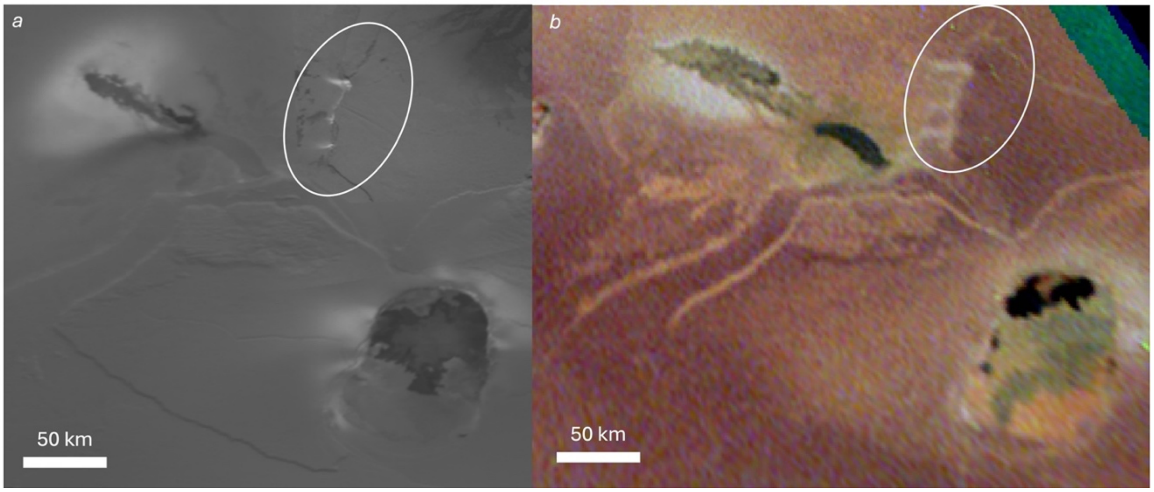

Figure 7. White diffuse deposits at scarp edge in Euboea Fluctus region does not appear to have changed in 44 year time interval between (a) *Voyager* 1 image and (b) JunoCam PJ58 Jupitershine image (JNCE_2024034_58C00025_V01). Images centered at 48° S, 14° E.

4 Discussion

The updated view of Io's surface, with favorable lighting geometry and resolution provided by Junocam imagery allows us to make more nuanced interpretations about the erosional processes acting on Io, informed by our terrestrial understanding of geomorphology and application to other worlds with higher resolution observations, like the Moon and Mars.

4.1 Contacts and Erosional Relationships from New Mapping Efforts

The new perspectives on Io's topography and geologic units afforded by the JunoCam imagery allow us to better constrain the relationships between mountain units, lava flows, and the surrounding plains. Though there have been many eruptions recorded on Io in the twenty years since Galileo captured imagery of Io's surface, there are no dramatic changes in shape to mountain slopes discernable in the JunoCam coverage. However, future imaging campaigns with a greater spatial overlap between high resolution datasets would be instrumental in better constraining the timing and dominant mechanisms of erosion on Io. The favorable lighting conditions and northern polar region coverage by JunoCam does allow us to update previous classifications of some mountains and paterae, improving our understanding of global relationships between surface features.

Jupitershine imagery of the Shamshu region provides new perspectives on a fascinating mountain-patera system that contains multiple mountain morphologies and clues to the tectonic progression that created the modern landscape. The now complete images of North and South Shamshu Mons in particular invite speculation about the timing of mountain formation and degradation. South and West Shamshu Montes have morphologically similar aprons of layered plains material, but if these were once one consistent plateau (like that in the North polar region), then they had to form before the large-scale rifting that created the modern configuration. If the layered plains formed from slope failure later, it is possible they formed at similar geologic times in order to create plains of similar degradation states. Furthermore, the blocky deposits visible on West Shamshu Mons' flanks indicate yet another later episode of degradation.

In the northern region, the mapped contacts between geologic units include certain and approximate contacts (where shadows or resolution limitations require the geometry of the contact to be inferred), as well as gradational contacts where the boundary between two units is transitional. This convention follows Williams et al. (2011), which notes that the contacts between lineated mountains or mottled mountains can be gradational with layered plains. In the northern map presented here, gradational contacts occur instead between lineated and mottled mountains. Globally, Io's mountains are characterized as either lineated or mottled, with some implications for level of degradation increasing with the mottled morphotype (Williams et al., 2011). While other regional studies do subdivide mountains (e.g., Bunte et al., 2008, 2010; Williams et al., 2004), the northern mountains capture in new detail the transition between these two phases. For both the northeast and southwest mountains, there are clear lobes of hummocky debris released downslope from the smooth ridges above, mapped as mottled mountain material. These hummocky lobes may eventually smooth out into layered plains material via diffusive processes, but we cannot be certain of this progression.

Ultimately, the superposition of the blocky deposit and mottled material atop layered plains, and the gradational transition between lineated and mottled mountain material, capture several stages of the depositional and erosional processes acting at different times across Io's surface.

4.2 Northern Block Formation

Because the blocky deposit of the northern mapping region is so distinctive, and contains such numerous blocks atop a >1 kilometer tall sloped plateau, it is worth exploring in more detail their possible formation mechanisms. Previous work detailing erosional processes on Io, particularly relating to mass wasting, do not entirely capture the morphology of the remaining material that is visible in the blocky deposit. For example, Schenk and Bulmer (1998) and Moore et al. (2001) discuss both large-scale landslides modifying mountainsides and smaller-scale basal debris cones from scarp retreat, but neither process results in the formation of kilometer-scale blocks. Here, we present several possible mechanisms to produce the observed feature morphology.

4.2.1 Erosional Remnant

In the mapped region, as well as elsewhere on Io, layered plains—consistent with their name—can occur as large slabs layered on top of each other, exposing multiple generations of material (see units p_{L1} vs. p_{L2}, Figure 4). Moore et al. (2001) and Schenk and Bulmer (1998) offer two possibilities for mountain-adjacent plateaus with lobate margins: they could be landslide deposits, or they could be formed from the uplift and lateral compression of a weak underlying surface layer. Given the height of the connected northern plateaus (>1km) and their outward sloping surfaces, the landslide interpretation may be more likely. However they formed, the margins of the layered plains units are eroding back, possibly via the debris cone and scalloped headwall processes defined by Moore et al. (2001). The slab-shaped proportions of the individual mesas of the blocky unit, as well as the elongate shape of the three largest blocks (with the long axis oriented nearly parallel to the adjacent scarp) could be consistent with a 0.5-1 km thick layered plains unit that has eroded away, leaving some of these blocks behind, in a process akin to the allochthonous sandstone boulders perched atop a plateau in the tableland of the Stołowe Mountains, Poland (e.g., Migoń & Parzóch, 2021). The mountain unit directly adjacent to the blocky deposit is mapped as mottled due to the presence of hummocky material closest to the proximal lineated mountain, but it also appears to have a uniform thickness (as estimated by the consistently illuminated bounding scarp on the east) and areas of smooth surface similar to the layered plains unit below. There are two blocks on top of this unit—perhaps a remnant of yet another plains layer—but the majority of the blocky deposit could be sourced from this plains unit.

If these blocks are erosional remnants, two questions must be raised: why were these blocks left behind, and where did the eroded material go? Differential erosion to leave the blocks behind as a lag would require some heterogeneity within the layered plains. There is nothing in their size, shape, distribution, or albedo to inform what those heterogeneities may be, though compositional differences—including interlayered SO_2 frost—would be the most likely source of strength differences. To interrogate material transport on Io, we must consider the relationship between the blocks and the underlying gently sloping plains. The existing body of literature pertaining to the process of creep on Io is concerned with viscous creep or relaxation within Io's crust (e.g., McKinnon et al., 2001; Ojakangas & Stevenson, 1986). Here, however, we must explore the slow, steady downslope movement of regolith via creep, modeled after diffusive hillslope processes on Earth. Io's surface, composed of lava flows, crustal blocks, and a thin mantling of SO_2 frost, is generally modeled as a solid. It is likely that the combination of volcanically-induced seismicity, chemical (and physical) interactions between condensing and sublimating frost, and bombardment from micrometeorites and volcanic byproducts, could contribute to rock weathering into regolith material, as it has been shown to do on Earth, Mars, and the Moon (Fassett & Thomson, 2014; Gilbert, 1909; Mantovani et al., 2014; Perron et al., 2003; Rapp, 1960; Xiao et al. (2013)) . If Io's plateaus are blanketed by even a thin layer of regolith (centimeters thick), and their surfaces are sloped >0 degrees, then they offer a mechanism to slowly translate plateau material downslope over geologic time to be eventually recycled by lava flows on the red-brown plains. Therefore, creep processes acting on Io's ~1.5 degree sloped plateau is a viable mechanism to erode the layered plains material away around the blocky deposit.

We also consider if regolith material could be transported away by wind. McDonald et al. (2022) propose a mechanism for aeolian sediment transport driven by sublimation vapor flows due to lava-SO_2 frost interactions, but the distance of the plateaus from the nearest lava flow would make it difficult for material up on the plateau to be affected by sustained winds under Io's sparse atmosphere.

4.2.2 Rockfall

The proximity of the blocky deposit to the lineated mountain material of West Cocytus Mons introduces the possibility that blocks are the product of rockfall, where large pieces of crust, triggered by gravity or seismic activity, broke up and tumbled down the more steeply sloping edifice to scatter across the gently sloping plateau surface. Dry rockfall is widely recognized as a mechanism for landscape evolution across the solar system, even on slopes below the angle of repose, from the Moon to Mars to Mercury (Beer et al., 2024; Cardenas et al., 2025; Conway et al., 2019; Fassett et al., 2017; Kokelaar et al., 2017). To investigate this possibility, we consider only the 41 blocks adjacent to the lineated mountain. Boulders and cobbles produced by rockfall on Earth are irregular, angular, and often characterized as polyhedral in shape, as they have had limited interactions for rounding (such as in fluvial transport) (e.g., Bonneau et al., 2019; Leine et al., 2014). Higher resolution coverage of this area would assist in characterizing the shape of Io's blocks; though they appear to have an angular shape in plan view, many blocks are only a few pixels in size, and therefore it is impossible to accurately determine the angularity (Figure 4). Terrestrial rockfall deposits can contain rocks with equant or cubic to elongate or platy shapes, determined by factors like rock type, fracture patterns, and weathering (e.g., Bonneau et al., 2019; Blott & Pye, 2008). The aspect ratio of the blocks—consistently much wider than they are tall—would be more indicative of sliding than tumbling and bouncing from the source region above (e.g. Lamb et al., 2015). However, regolith redistribution via creep as outlined in Section 4.1.1 could partially bury the lower portions of the blocks, causing an apparent decrease in height over geologic time. In an alternative interpretation, block emplacement was concurrent with the mass wasting processes that formed the layered plains material, and the large blocks simply made their way to the top of the poorly sorted sediment mixture, due to kinetic sieving (e.g. Marc et al, 2021). If this were the case, we would expect a block size distribution increasing in frequency as size decreases, with a large population of blocks just at the limit of resolvability. The spatial and size distribution of the blocks—without such a large population of small blocks—does not support this single event landslide model.

If these blocks did tumble down from the nearest approximated "summit" onto the plateau below as in Figure 5, they might demonstrate a common terrestrial relationship: larger blocks tend to have longer runout distances due to greater momentum and resilience to breakage (e.g., Corominas et al., 2019). However, the blocky deposit has no significant relationship between block size and runout distance, and some of the largest blocks have the smallest runout distance (Figure 5). Moreover, there is no evidence for tracks or bounce and skip marks discernable at the JunoCam resolution, though these features are only visible for recent rockfall events on Earth, quickly erased by vegetation, fluvial erosion, and hillslope processes.

4.2.3 Outrunner Blocks

Io's blocks are 2-3 orders of magnitude larger and 2-3 orders of magnitude farther from the nearest source area as compared to terrestrial rockfall blocks, though Io's gravity is ~18% that of Earth's, negating some of this distance discrepancy. On Earth, large, lithified blocks associated with submarine landslides can detach from the debris toe and glide along the seafloor, lubricated by a thin layer of seawater (e.g., De Blasio et al., 2006; Mohrig et al., 1998). Outrunner blocks have been described across the world, from the Nigerian Sea (Nissen et al., 1999) to the Faeroe basin (Kuijpers et al., 2001; Nielsen & Kuijpers, 2004) and the Taranaki basin, New Zealand (Rusconi, 2017). The megaclasts in these deposits can be up to 400 meters tall, 1.9 km long, and 1.2 km wide—a similar size and shape to the blocky deposits (Figure 5). Moreover, there are instances in the Faeroe basin of megaclasts traveling 25 km on a slope less than 1 degree (Nielsen & Kuijpers, 2004), which parallels the 40-120 km runout distances across a slope of a few degrees of the blocky deposit.

Water is not the only lubricant to move large volumes of rock over shallow slopes. Wyoming's Heart Mountain is an enigmatic block of 500-350 million-year-old limestone sitting on top of much younger ~55 million-year-old clastic sedimentary rock, detached from the closest rocks of this unit by ~50 km. The geologic history of the Heart Mountain block is debated, but several interpretations for its formation suggest that it is the product of the largest terrestrial landslide ever recorded, where it's massive size and runout distance over a shallow 2° slope was enabled by lubrication: one hypothesis calls for "hovercraft" floatation on volcanic gases associated with the active Absaroka volcanic province (Hughes, 1970; Beutner & Craver, 1996), while another model proposes basal frictional heating could reach high enough temperatures to calcine the carbonate rock, producing calcium and magnesium oxide powders that could become fluidized by the byproduct pressurized carbon dioxide gas in order to reduce friction for the block to slide (Anders et al., 2010). Yet another interpretation involves an acoustic fluidization process, where a 40-meter-long sound wave trapped just beneath the fault contributed to particle flow as a non-Newtonian fluid at the base of the translating slab (Melosh, 1983).

While both of these megaclast examples provide tidy morphological analogs to Io's blocky deposit, the lubrication mechanism is far less clear. There is no evidence for volcanism directly neighboring these features to provide a heating source, and frictional heating of SO_2 frost (of unknown thickness) to create a gaseous layer to glide on would be unlikely on such shallow slopes.

4.2.4 Cliff Collapse

While this study primarily focuses on the population of blocks adjacent to the West Cocytus Mons, there are six individual blocks mapped adjacent to and below the tall, >1 km high scarps of the layered plains. The simplest model for their association is that the blocks are derived from the layered plains, and large segments cleave off of the cliff, hinging down to the plains below in a cliff collapse process. This scarp erosion mechanism differs from the Type D (debris cone) or Type T (terraced) slopes defined by Moore et al. (2001), because it requires fracturing parallel to the scarp and reflects a greater degree of cohesion, as large blocks remain intact instead of producing smaller scale rockfall debris piles. If all blocks in the blocky deposit unit share a common origin, these marginal blocks may capture this erosional process in action. The population of blocks adjacent to West Cocytus Mons could be the remnant collapse blocks of a now-receded scarp, slowly eroding down into the plains. This variation on the Section 4.1.1 erosional remnant model does not require heterogeneities intrinsic in the crustal layers; the blocks reflect original fracturing size, not erosional resistance. Likewise, the size and aspect ratio of the blocks is consistent with flaking slabs of cliff material.

4.2.5 Endogenic Formation Mechanisms

For completeness, we also consider whether the blocky deposit could have formed in situ from endogenic processes. Though Io's volcanism is concentrated in its paterae, could these blocks be edifices resulting from another magmatic process?

Rhyolite domes form isolated or clustered edifices on Earth due to the slow extrusion of very viscous silicic lava. They generally do not have craters, and can grow as large as Lassen Peak (~3 km tall). There is no evidence for high silica content on Io, as all observed volcanism is hot and mafic, but could be present in local environments if magma ascent is stalled in the cold lithosphere and fractional crystallization is permitted to progress.

Rootless cones, such as those dotting the shore of Lake Mývatn, Iceland, are another smaller-scale, multiple-edifice volcanic construct. These pseudocraters form when lava flows over saturated ground, resulting in explosive phreatomagmatic eruptions as water vaporizes, so they are not connected by a magmatic "root" (e.g., Fagents & Thordarson, 2007). Similar features have been identified on Mars as the result of lava interactions with subsurface water ice (Fagents et al., 2002; Fagents & Thordarson, 2007). Though no central craters can be identified at the JunoCam resolution, their presence cannot be ruled out. The distribution of blocks is also perhaps more consistent with rootless cone clustering on Earth and Mars than the random distribution of an impact crater field (Bruno et al., 2004). While the phreatomagmatic process boasts some similarities to the sublimation of SO_2 frost at the toe of Io's lava flows, the absence of lava flows across the layered plains yield this formation mechanism unlikely.

4.2.6 A Ranking of Preferred Erosional Mechanisms

All mechanisms presented here are variably feasible, though some are included more for completeness than serious consideration. The endogenic formation mechanisms can be ruled out, since the morphologies of the blocks, as well as their distribution (at cliff edges as well as distributed across layered plains), at least at the current resolution, are inconsistent with the volcanic edifices we see on Earth.

Outrunner blocks, while a much better morphological match for the blocks, are an unlikely mechanism, due to the unknown processes necessary to raft the blocks across a shallow slope on Io. While this fun and complex processes could be a possibility, the simplest mechanism is often the more likely explanation.

An erosional remnant, while possible due to the viability of regolith generation and creep on Io, would need to develop over geologic time. Without any known sources for crustal heterogeneities necessary to produce something like the isolated blocks, we must invoke a process like rockfall with subsequent regolith generation and surface evolution. The distribution of blocks across the plains, as measured from the nearest "summit" does not follow standard terrestrial relationships. Therefore, we consider the combined rockfall and subsequent partial burial of the blocks to be possible.

Ultimately, our preferred formation mechanism for the blocky deposit is cliff collapse. The multiple generations of layered plains preserved in the mapped region provide a likely source of material, and scarp edges deteriorating into large blocks at the margins of these plains demonstrate how such a process could easily produce blocks of the observed proportions. Heterogeneities in the block distribution depend more on the weathering processes driving scarp retreat, which is reasonable.

5 Conclusions

Juno’s PJ57 and PJ58s flybys of Io produced spectacular imagery that provides a new perspective on the previously unresolved north polar region of the moon. The low solar incidence angle captured Io’s dramatic topography in a new light, allowing us to identify 10 previously mapped features that should be reclassified now that their topographical relationship to the surrounding units is more evident. PJ58 Jupitershine coverage of the Shamshu Patera region further clarifies mountain-patera relationships, and allows us to expand on previously proposed tectonic reconstructions of that region to incorporate similar mountain morphologies separated by rifted plains.

Three polar mountains in particular, connected by several generations of layered plains material, exhibit a greater degree of morphological complexity than can normally be identified in Io’s mountains. We present a regional geologic map of this trio that allows us to investigate the relationships between mountain units and degradation states more closely. While the mapped geologic units are consistent with the global paradigm defined by Williams et al. (2010), a new unit is required to describe a unique blocky deposit blanketing the inter-mountain plateau. While similar blocks do appear elsewhere on Io, their abundance in the JunoCam imagery, and relationship with the surrounding geologic units, allows us to interrogate several possible formation mechanisms for these blocks: an erosional remnant, rockfall debris, outrunner blocks, cliff collapse slabs, or endogenic features like rhyolite domes or rootless cones. While there are consistencies and inconsistencies with all of these mechanisms, a combination of cliff collapse slabs with regolith creep is the most plausible.

Ultimately, the JunoCam images of the north polar mountains capture a new perspective on Io’s surface evolution. Lineated mountains are collapsing into mottled mountain material in discrete lobes that extend out on to the layered plains. Layered plains themselves are built with multiple generations overlying each other, forming shallowly sloped plateaus. Blocky deposits sitting atop and at the collapsing margins of these sloped surfaces require even later modification and continual erosion. This new imagery captures an important intermediate stage in the formation and erosion of tectonic features on a volcanic world; what was once an unresolvable smear has become a portrait of Io's dynamic surface erosion in action.

Acknowledgments

We thank NASA, *Juno* mission PI Scott Bolton and the *Juno* team, and in particular the JunoCam instrument team including PI Candy Hansen and Mike Ravine, for acquiring the images of Io used in this study as part of *Juno's* extended mission. We also thank David Crown for the thorough review that improved the clarity of the paper, as well as thesis committee members Mike Lamb, John Grotzinger, and Bethany Ehlmann for their helpful Earth and planetary perspective on the proposed erosional mechanisms. This work was partially supported by NASA's New Frontiers Data Analysis Program and the NASA ROSES Solar System Workings program through task order 80NM0018F0612. Part of this work was performed at the Jet Propulsion Laboratory, California Institute of Technology, under contract to NASA.

Data Availability Statement

JunoCam data presented in this work are archived and freely available to the public in the NASA Planetary Data System (PDS) Imaging Node in PDS3 format. (Caplinger, 2014). NAIF SPICE kernels are used to navigate JIRAM and JunoCam observations and are available publicly in the PDS Navigation and Ancillary Information Facility (NAIF) (Semenov et al., 2017). An integrated ArcGIS database containing *Voyager* and *Galileo* coverage of Io can be downloaded from the Arizona State University Ronald Greeley Center for Planetary Studies (https://rgcps.asu.edu/gis_data/). Block measurements used in this study can be found in Supplementary Data Table S1.

References

Anders, M. H., Fouke, B. W., Zerkle, A. L., Tavarnelli, E., Alvarez, W., & Harlow, G. E. (2010). The role of calcining and basal fluidization in the long runout of carbonate slides: an example from the Heart Mountain slide block, Wyoming and Montana, USA. *The Journal of Geology*, *118*(6), 577-599. https://doi.org/10.1086/656383

Anderson, R. S., & Anderson, S. P. (2010). *Geomorphology: The mechanics and chemistry of landscapes*. Cambridge University Press.

Beer, A. R., Fischer, J. N., Ulizio, T. P., Ma, Z., Sun, Z., & Lamb, M. P. (2024). A mechanistic model and experiments on bedrock incision and channelization by rockfall. *Journal of Geophysical Research: Earth Surface*, *129*(3), e2023JF007504. https://doi.org/10.1029/2023JF007504

Beutner, E. C., & Craven, A. E. (1996). Volcanic fluidization and the Heart Mountain detachment, Wyoming. *Geology*, *24*(7), 595-598. https://doi.org/10.1130/0091-7613(1996)024<0595:VFATHM>2.3.CO;2

Blott, S. J., & Pye, K. (2008). Particle shape: a review and new methods of characterization and classification. *Sedimentology*, *55*(1), 31-63. https://doi.org/10.1111/j.1365-3091.2007.00892.x

Bonneau, D. A., Hutchinson, D. J., DiFrancesco, P. M., Coombs, M., & Sala, Z. (2019). Three-dimensional rockfall shape back analysis: Methods and implications. *Natural Hazards and Earth System Sciences*, *19*(12), 2745-2765. https://doi.org/10.5194/nhess-19-2745-2019

Bruno, B. C., Fagents, S. A., Thordarson, T., Baloga, S. M., & Pilger, E. (2004). Clustering within rootless cone groups on Iceland and Mars: Effect of nonrandom processes. *Journal of Geophysical Research: Planets*, *109*(E7). https://doi.org/10.1029/2004JE002273

Bunte, M. K., Williams, D. A., & Greeley, R. (2008). Geologic mapping of the Zal region of Io. *Icarus*, *197*(1), 354-367. https://doi.org/10.1016/j.icarus.2008.04.013

Bunte, M. K., Williams, D. A., Greeley, R., & Jaeger, W. L. (2010). Geologic mapping of the Hi'iaka and Shamshu regions of Io. *Icarus*, *207*(2), 868-886. doi:10.1016/j.icarus.2009.12.006

Caplinger, M. (2014). Juno JunoCam EDR V1.0 [Dataset]. *NASA Planetary Data System*. https://doi.org/10.17189/1520191

Cardenas, B. T., Beer, A. R., Donohoe, P. J., Kanine, O., Dickson, J. L., & Lamb, M. P. (2025). Crater-wall degradation and bedrock-chute formation from dry rockfall erosion. *Geology*, *53*(5), 456-460. https://doi.org/10.1130/G53096.1

Carlson, R. W., Smythe, W. D., Lopes-Gautier, R. M. C., Davies, A. G., Kamp, L. W., Mosher, J. A., ... & Fanale, F. P. (1997). The distribution of sulfur dioxide and other infrared absorbers on the surface of Io. *Geophysical Research Letters*, *24*(20), 2479-2482. https://doi.org/10.1029/97GL02609

Carr, M. H., McEwen, A. S., Howard, K. A., Chuang, F. C., Thomas, P., Schuster, P., ... & *Galileo* Imaging Team. (1998). Mountains and calderas on Io: Possible implications for lithosphere structure and magma generation. *Icarus*, 135(1), 146-165. Reclassified geologic units based on JunoCam imagery. https://doi.org/10.1006/icar.1998.5979

Conway, S. J., de Haas, T., & Harrison, T. N. (2019). Martian gullies: A comprehensive review of observations, mechanisms and insights from Earth analogues. *Martian Gullies and their Earth Analogues: Geological Society, London, Special Publication* 467, 7–66. https://doi.org/10.1144/SP467.14.

Corominas, J., Matas, G., & Ruiz-Carulla, R. (2019). Quantitative analysis of risk from fragmental rockfalls. *Landslides*, *16*(1), 5-21. https://doi.org/10.1007/s10346-018-1087-9

Crown, D.A., Greeley, R., Craddock, R.A., & Schaber, G.G. (1992). *Geologic map of Io*. US Department of the Interior, US Geological Survey.

Davies, A. G. (2007) Volcanism on Io: a Comparison with Earth. Cambridge University Press, Cambridge, UK. 372 pages.

Davies, A. G., Keszthelyi, L. P., & Harris, A. J. (2010). The thermal signature of volcanic eruptions on Io and Earth. *Journal of Volcanology and Geothermal Research*, *194*(4), 75-99. https://doi.org/10.1016/j.jvolgeores.2010.04.009

Davies, A. G., Keszthelyi, L. P., Williams, D. A., Phillips, C. B., McEwen, A. S., Lopes, R. M., ... & Carlson, R. W. (2001). Thermal signature, eruption style, and eruption evolution at Pele and Pillan on Io. *Journal of Geophysical Research: Planets*, *106*(E12), 33079-33103. https://doi.org/10.1029/2000JE001357

Davies, A. G., Perry, J. E., Williams, D. A., Veeder, G. J., & Nelson, D. M. (2024). New global map of Io's volcanic thermal emission and discovery of hemispherical dichotomies. *The Planetary Science Journal*, *5*(5), 121. https://doi.org/10.3847/PSJ/ad4346

Davies, A. G., Wilson, L., Matson, D., Leone, G., Keszthelyi, L., & Jaeger, W. (2006). The heartbeat of the volcano: The discovery of episodic activity at Prometheus on Io. *Icarus*, *184*(2), 460-477. doi:10.1016/j.icarus.2006.05.012.

De Blasio, F. V., Engvik, L. E., & Elverhøi, A. (2006). Sliding of outrunner blocks from submarine landslides. *Geophysical Research Letters*, *33*(6). https://doi.org/10.1029/2005GL025165

de Kleer, K., de Pater, I., Molter, E. M., Banks, E., Davies, A. G., Alvarez, C., ... & Tollefson, J. (2019a). Io’s volcanic activity from time domain adaptive optics observations: 2013–2018. *The Astronomical Journal*, *158*(1), 29. https://doi.org/10.3847/1538-3881/ab2380

de Kleer, K., Nimmo, F., & Kite, E. (2019b). Variability in Io's volcanism on timescales of periodic orbital changes. *Geophysical Research Letters*, *46*(12), 6327-6332. https://doi.org/10.1029/2019GL082691

de Pater, I., de Kleer, K., Davies, A. G., & Ádámkovics, M. (2017). Three decades of Loki Patera observations. *Icarus*, *297*, 265-281. https://doi.org/10.1016/j.icarus.2017.03.016

de Pater, I., Keane, J. T., de Kleer, K., & Davies, A. G. (2021). A 2020 observational perspective of Io. *Annual Review of Earth and Planetary Sciences*, *49*(1), 643-678. https://doi.org/10.1146/annurev-earth-082420-095244

Douté, S., Schmitt, B., Lopes-Gautier, R., Carlson, R., Soderblom, L., Shirley, J., & Galileo NIMS Team. (2001). Mapping SO2 frost on Io by the modeling of NIMS hyperspectral images. *Icarus*, *149*(1), 107-132. https://doi.org/10.1006/icar.2000.6513

Fagents, S. A., & Thordarson, T. (2007). Rootless volcanic cones in Iceland and on Mars. *The Geology of Mars: Evidence from Earth-based Analogs*, 151-177.

Fagents, S. A., Lanagan, P., & Greeley, R. (2002). Rootless cones on Mars: A consequence of lava-ground ice interaction. *Geological Society, London, Special Publications*, *202*(1), 295-317. https://doi.org/10.1144/GSL.SP.2002.202.01.15

Fassett, C. I., Crowley, M. C., Leight, C., Dyar, M. D., Minton, D. A., Hirabayashi, M., ... & Watters, W. A. (2017). Evidence for rapid topographic evolution and crater degradation on Mercury from simple crater morphometry. *Geophysical Research Letters*, *44*(11), 5326-5335. https://doi.org/10.1002/2017GL073769

Fassett, C. I., & Thomson, B. J. (2014). Crater degradation on the lunar maria: Topographic diffusion and the rate of erosion on the Moon. *Journal of Geophysical Research: Planets*, *119*(10), 2255-2271. https://doi.org/10.1002/2014JE004698

Geissler, P. E., McEwen, A. S., Keszthelyi, L., Lopes-Gautier, R., Granahan, J., & Simonelli, D. P. (1999). Global color variations on Io. *Icarus*, *140*(2), 265-282. https://doi.org/10.1006/icar.1999.6128

Geissler, P., McEwen, A., Phillips, C., Keszthelyi, L., & Spencer, J. (2004). Surface changes on Io during the *Galileo* mission. *Icarus*, *169*(1), 29-64. https://doi.org/10.1016/j.icarus.2003.09.024

Gilbert, G. K. (1909). The convexity of hilltops. *The Journal of Geology*, *17*(4), 344-350. https://doi.org/10.1086/621620

Highland, L. M., & Bobrowsky, P. (2008). *The landslide handbook-A guide to understanding landslides* (No. 1325). US Geological Survey.

Hughes, C. J. (1970). The Heart Mountain detachment fault: A volcanic phenomenon? *The Journal of Geology*, *78*(1), 107-116. https://doi.org/10.1086/627491

Jaeger, W. L., Turtle, E. P., Keszthelyi, L. P., Radebaugh, J., McEwen, A. S., & Pappalardo, R. T. (2003). Orogenic tectonism on Io. *Journal of Geophysical Research: Planets*, *108*(E8). https://doi.org/10.1029/2002JE001946

Johnson, R. E. (1997). Polar "caps" on Ganymede and Io revisited. *Icarus*, *128*(2), 469-471. https://doi.org/10.1006/icar.1997.5746

Johnson, T. V., Cooke, I. I., Sagan, C., & Soderblom, L. A. (1979). Volcanic resurfacing rates and implications for volatiles on Io. *Nature (London);(United Kingdom)*, *280*(5725). https://doi.org/10.1038/280746a0

Keszthelyi, L., Jaeger, W., Milazzo, M., Radebaugh, J., Davies, A. G., & Mitchell, K. L. (2007). New estimates for Io eruption temperatures: Implications for the interior. *Icarus*, *192*(2), 491-502. https://doi.org/10.1016/j.icarus.2007.07.008

Keszthelyi, L., Jaeger, W. L., Turtle, E. P., Milazzo, M., & Radebaugh, J. (2004). A post-*Galileo* view of Io's interior. *Icarus*, *169*(1), 271-286. https://doi.org/10.1016/j.icarus.2004.01.005

Keszthelyi, L., McEwen, A. S., Phillips, C. B., Milazzo, M., Geissler, P., Turtle, E. P., ... & Denk, T. (2001). Imaging of volcanic activity on Jupiter's moon Io by *Galileo* during the Galileo Europa Mission and the Galileo Millennium Mission. *Journal of Geophysical Research: Planets*, *106*(E12), 33025-33052. https://doi.org/10.1029/2000JE001383

Kieffer, S. W., Lopes-Gautier, R., McEwen, A., Smythe, W., Keszthelyi, L., & Carlson, R. (2000). Prometheus: Io's wandering plume. *Science*, *288*(5469), 1204-1208. DOI: 10.1126/science.288.5469.1204

Kirchoff, M. R., & McKinnon, W. B. (2009). Formation of mountains on Io: Variable volcanism and thermal stresses. *Icarus*, *201*(2), 598-614. https://doi.org/10.1016/j.icarus.2009.02.006

Kokelaar, B. P., Bahia, R. S., Joy, K. H., Viroulet, S., & Gray, J. M. N. T. (2017). Granular avalanches on the Moon: Mass-wasting conditions, processes, and features. *Journal of Geophysical Research: Planets*, *122*(9), 1893-1925. https://doi.org/10.1002/2017JE005320

Kuijpers, A., Nielsen, T., Akhmetzhanov, A., De Haas, H., Kenyon, N., & van Weering, T. (2001). Late Quaternary slope instability on the Faeroe margin: mass flow features and timing of events. *Geo-Marine Letters*, *20*, 149-159. https://doi.org/10.1007/s003670000053

Lamb, M. P., Finnegan, N. J., Scheingross, J. S., & Sklar, L. S. (2015). New insights into the mechanics of fluvial bedrock erosion through flume experiments and theory. *Geomorphology*, *244*, 33-55. https://doi.org/10.1016/j.geomorph.2015.03.003

Leone, G., Davies, A. G., Wilson, L., Williams, D. A., Keszthelyi, L. P., Jaeger, W. L., & Turtle, E. P. (2009). Volcanic history, geologic analysis and map of the Prometheus Patera region on Io. *Journal of Volcanology and Geothermal Research*, *187*(1-2), 93-105. https://doi.org/10.1016/j.jvolgeores.2009.07.019

Leine, R. I., Schweizer, A., Christen, M., Glover, J., Bartelt, P., & Gerber, W. (2014). Simulation of rockfall trajectories with consideration of rock shape. *Multibody System Dynamics*, *32*, 241-271. https://doi.org/10.1007/s11044-013-9393-4

Lindsay, J. (1976). Energy at the lunar surfaces. In *Lunar stratigraphy and sedimentology* (Vol. 3, pp. 45-55). Amsterdam, The Netherlands: Elsevier.

Lopes, R. M., de Kleer, K., & Keane, J. T. (Eds.). (2023). *Io: A new view of Jupiter's Moon*. Springer. https://doi.org/10.1007/978-3-031-25670-7

Lopes, R. M., Kamp, L. W., Douté, S., Smythe, W. D., Carlson, R. W., McEwen, A. S., ... & Soderblom, L. A. (2001). Io in the near infrared: Near-Infrared Mapping Spectrometer (NIMS) results from the *Galileo* flybys in 1999 and 2000. *Journal of Geophysical Research: Planets*, *106*(E12), 33053-33078. https://doi.org/10.1029/2000JE001463

Mantovani, J. G., Swanger, A., Townsend III, I. I., Sibille, L., & Galloway, G. (2014). Characterizing the physical and thermal properties of planetary regolith at low temperatures. *Earth and Space 2014*, 43-51. https://doi.org/10.1061/9780784479179.006

Marc, O., Turowski, J. M., & Meunier, P. (2021). Controls on the grain size distribution of landslides in Taiwan: The influence of drop height, scar depth and bedrock strength. *Earth Surface Dynamics*, *9*(4), 995-1011. https://doi.org/10.5194/esurf-9-995-2021

McCauley, J. F., Smith, B. A., & Soderblom, L. A. (1979). Erosional scarps on Io. *Nature*, *280*(5725), 736-738. https://doi.org/10.1038/280736a0

McDonald, G. D., Méndez Harper, J., Ojha, L., Corlies, P., Dufek, J., Ewing, R. C., & Kerber, L. (2022). Aeolian sediment transport on Io from lava–frost interactions. *Nature Communications*, *13*(1), 2076. https://doi.org/10.1038/s41467-022-29682-x

McEwen, A. S. (1988). Global color and albedo variations on Io. *Icarus*, *73*(3), 385-426. https://doi.org/10.1016/0019-1035(88)90053-X

McEwen, A. S., Keszthelyi, L., Geissler, P., Simonelli, D. P., Carr, M. H., Johnson, T. V., ... & Schubert, G. (1998). Active volcanism on Io as seen by *Galileo* SSI. *Icarus*, *135*(1), 181-219. https://doi.org/10.1006/icar.1998.5972

McEwen, A. S., Keszthelyi, L. P., Lopes, R., Schenk, P. M., & Spencer, J. R. (2004). The lithosphere and surface of Io. *Jupiter: The Planet, Satellites and Magnetosphere*, 1, 307-328.

McEwen, A. S., & Soderblom, L. A. (1983). Two classes of volcanic plumes on Io. *Icarus*, *55*(2), 191-217. https://doi.org/10.1016/0019-1035(83)90075-1

McKinnon, W. B., Schenk, P. M., & Dombard, A. J. (2001). Chaos on Io: A model for formation of mountain blocks by crustal heating, melting, and tilting. *Geology*, *29*(2), 103-106. https://doi.org/10.1130/0091-7613(2001)029<0103:COIAMF>2.0.CO;2

Melosh, H. J. (1983). Acoustic fluidization: can sound waves explain why dry rock debris appears to flow like a fluid in some energetic geologic events?. *American Scientist*, *71*(2), 158-165. https://www.jstor.org/stable/27851899

Melosh, H. J. (2011). *Planetary surface processes* (Vol. 13). Cambridge University Press.

Migoń, P., & Parzóch, K. (2021). Enigmatic sandstone boulder clusters on the plateaus of the Stołowe Mts.–their geoheritage and geotourism value. *Geologos*, *27*, 141-155. DOI: 10.2478/logos-2021-0017

Milazzo, M. P., Keszthelyi, L. P., & McEwen, A. S. (2001). Observations and initial modeling of lava-SO2 interactions at Prometheus, Io. *Journal of Geophysical Research: Planets*, *106*(E12), 33121-33127. https://doi.org/10.1029/2000JE001410

Mohrig, D., Ellis, C., Parker, G., Whipple, K. X., & Hondzo, M. (1998). Hydroplaning of subaqueous debris flows. *Geological Society of America Bulletin*, *110*(3), 387-394. https://doi.org/10.1130/0016-7606(1998)110<0387:HOSDF>2.3.CO;2

Moore, J. M., Sullivan, R. J., Chuang, F. C., Head III, J. W., McEwen, A. S., Milazzo, M. P., ... & Turtle, E. P. (2001). Landform degradation and slope processes on Io: The

Galileo view. *Journal of Geophysical Research: Planets*, *106*(E12), 33223-33240. https://doi.org/10.1029/2000JE001375

Nissen, S. E., Haskell, N. L., Steiner, C. T., & Coterill, K. L. (1999). Debris flow outrunner blocks, glide tracks, and pressure ridges identified on the Nigerian continental slope using 3-D seismic coherency. *The Leading Edge*, *18*(5), 595-599. https://doi.org/10.1190/1.1438343

Nielsen, T., & Kuijpers, A. (2004). Geohazard studies offshore the Faroe Islands: slope instability, bottom currents and sub-seabed sediment mobilisation. *GEUS Bulletin*, *4*, 57-60. https://doi.org/10.34194/geusb.v4.4785

Ojakangas, G. W., & Stevenson, D. J. (1986). Episodic volcanism of tidally heated satellites with application to Io. *Icarus*, *66*(2), 341-358. https://doi.org/10.1016/0019-1035(86)90163-6

O'Reilly, T. C., & Davies, G. F. (1981). Magma transport of heat on Io: A mechanism allowing a thick lithosphere. *Geophysical Research Letters*, *8*(4), 313-316. https://doi.org/10.1029/GL008i004p00313

Peale, S. J., Cassen, P., & Reynolds, R. T. (1979). Melting of Io by tidal dissipation. *Science*, *203*(4383), 892-894. DOI: 10.1126/science.203.4383.892

Park, R. S., Jacobson, R. A., Gomez Casajus, L., Nimmo, F., Ermakov, A. I., Keane, J. T., ... & Bolton, S. J. (2024). Io’s tidal response precludes a shallow magma ocean. *Nature*, 1-3. https://doi.org/10.1038/s41586-024-08442-5

Perron, J. T., Dietrich, W. E., Howard, A. D., McKean, J. A., & Pettinga, J. R. (2003). Ice-driven creep on Martian debris slopes. *Geophysical Research Letters*, *30*(14). https://doi.org/10.1029/2003GL017603

Perry, J.E., Davies, A.G., Williams, D.A., & Nelson, D.M. (2024) Tonatiuh: A new eruptive volcanic center on Io as seen by Juno/JIRAM. *LPI Contributions*, 3040, 1617. https://www.hou.usra.edu/meetings/lpsc2024/pdf/1617.pdf

Perry, J.E., Heyd, R., Read, M., Tornabene, L.L., … & Berry, K. (2022). Geometric processing of TGO CaSSIS observations. *Planetary and Space Science*, 223, 105581. https://doi.org/10.1016/j.pss.2022.105581

Radebaugh, J., Keszthelyi, L. P., McEwen, A. S., Turtle, E. P., Jaeger, W., & Milazzo, M. (2001). Paterae on Io: A new type of volcanic caldera? *Journal of Geophysical Research: Planets*, *106*(E12), 33005-33020. https://doi.org/10.1029/2000JE001406

Radebaugh, J., McEwen, A. S., Milazzo, M. P., Keszthelyi, L. P., Davies, A. G., Turtle, E. P., & Dawson, D. D. (2004). Observations and temperatures of Io's Pele Patera from

Cassini and *Galileo* spacecraft images. *Icarus*, *169*(1), 65-79. https://doi.org/10.1016/j.icarus.2003.10.019

Rapp, A. (1960). Recent development of mountain slopes in Kärkevagge and surroundings, northern Scandinavia. *Geografiska Annaler*, *42*(2-3), 65-200. https://doi.org/10.1080/20014422.1960.11880942

Rathbun, J. A., Spencer, J. R., Lopes, R. M., & Howell, R. R. (2014). Io's active volcanoes during the New Horizons era: Insights from New Horizons imaging. *Icarus*, 231, 261-272. https://doi.org/10.1016/j.icarus.2013.12.002

Ravine, M. A., Hansen, C. J., Caplinger, M. A., Schenk, P. M., Lipkaman Vittling, L., Krysak, D. J., ... & Bolton, S. J. (2024). JunoCam images of Io. *LPI Contributions*, *3040*, 1718. https://www.hou.usra.edu/meetings/lpsc2024/pdf/1718.pdf

Rodriguez, K. (2024). Integrated Software for Imagers and Spectrometers (ISIS) 8.3.0. U.S. Geological Survey. doi: 10.5066/p13tads5

Rusconi, F. J. (2017). *3D seismic interpretation of a Plio-Pleistocene mass transport deposit in the deepwater Taranaki basin of New Zealand*. University of Arkansas.

Schenk, P. M., & Bulmer, M. H. (1998). Origin of mountains on Io by thrust faulting and large-scale mass movements. *Science*, *279*(5356), 1514-1517. DOI: 10.1126/science.279.5356.1514

Schenk, P., Hargitai, H., Wilson, R., McEwen, A., & Thomas, P. (2001). The mountains of Io: Global and geological perspectives from *Voyager* and *Galileo*. *Journal of Geophysical Research: Planets*, *106*(E12), 33201-33222. https://doi.org/10.1029/2000JE001408

Semenov, B.V., Acton, C.H., Costa Sitja, M., Bailey, A.M. (2017). JUNO SPICE KERNELS V1.0 [Dataset]. *NASA Planetary Data System*. https://doi.org/10.17189/1520117

Spencer, D. C., Katz, R. F., & Hewitt, I. J. (2020). Magmatic intrusions control Io's crustal thickness. *Journal of Geophysical Research: Planets*, *125*(6), e2020JE006443. https://doi.org/10.1029/2020JE006443

Turtle, E. P., Jaeger, W. L., Keszthelyi, L. P., McEwen, A. S., Milazzo, M., Moore, J., ... & Schuster, P. (2001). Mountains on Io: High-resolution *Galileo* observations, initial interpretations, and formation models. *Journal of Geophysical Research: Planets*, *106*(E12), 33175-33199. https://doi.org/10.1029/2000JE001354

Turtle, E. P., Keszthelyi, L. P., McEwen, A. S., Radebaugh, J., Milazzo, M., Simonelli, D. P., ... & *Galileo* SSI Team. (2004). The final *Galileo* SSI observations of Io: orbits G28-I33. *Icarus*, *169*(1), 3-28. https://doi.org/10.1016/j.icarus.2003.10.014

Veeder, G. J., Matson, D. L., Johnson, T. V., Blaney, D. L., & Goguen, J. D. (1994). Io's heat flow from infrared radiometry: 1983–1993. *Journal of Geophysical Research: Planets*, *99*(E8), 17095-17162. https://doi.org/10.1029/94JE00637

Williams, D. A., Keszthelyi, L. P., Crown, D. A., Jaeger, W. L., & Schenk, P. M. (2007). Geologic mapping of the Amirani–Gish Bar region of Io: Implications for the global geologic mapping of Io. *Icarus*, *186*(1), 204-217. https://doi.org/10.1016/j.icarus.2006.08.023

Williams, D. A., Keszthelyi, L. P., Crown, D. A., Yff, J. A., Jaeger, W. L., Schenk, P. M., ... & Becker, T. L. (2011). *Geologic map of Io*. US Department of the Interior, US Geological Survey.

Williams, D. A., Keszthelyi, L. P., Crown, D. A., Yff, J. A., Jaeger, W. L., Schenk, P. M., ... & Becker, T. L. (2011). Volcanism on Io: New insights from global geologic mapping. *Icarus*, *214*(1), 91-112. https://doi.org/10.1016/j.icarus.2011.05.007

Williams, D. A., Keszthelyi, L. P., Schenk, P. M., Milazzo, M. P., Lopes, R. M., Rathbun, J. A., & Greeley, R. (2005). The Zamama–Thor region of Io: Insights from a synthesis of mapping, topography, and *Galileo* spacecraft data. *Icarus*, *177*(1), 69-88. https://doi.org/10.1016/j.icarus.2005.03.005

Williams, D. A., Perry, J. E., Nelson, D. M., & Davies, A. G. (2024). Updating Io's North Polar Geologic Map Using JunoCAM Images. *LPI Contributions*, *3044*, 7001. https://www.hou.usra.edu/meetings/pgm2024/pdf/7001.pdf

Williams, D. A., Radebaugh, J., Keszthelyi, L. P., McEwen, A. S., Lopes, R. M., Douté, S., & Greeley, R. (2002). Geologic mapping of the Chaac-Camaxtli region of Io from *Galileo* imaging data. *Journal of Geophysical Research: Planets*, *107*(E9), 6-1. https://doi.org/10.1029/2001JE001821

Williams, D. A., Schenk, P. M., Moore, J. M., Keszthelyi, L. P., Turtle, E. P., Jaeger, W. L., ... & Greeley, R. (2004). Mapping of the Culann–Tohil region of Io from *Galileo* imaging data. *Icarus*, *169*(1), 80-97. https://doi.org/10.1016/j.icarus.2003.08.024

Xiao, Z., Zeng, Z., Ding, N., & Molaro, J. (2013). Mass wasting features on the Moon–how active is the lunar surface? *Earth and Planetary Science Letters*, *376*, 1-11. https://doi.org/10.1016/j.epsl.2013.06.015

Supplementary Data for Chapter 3

This section contains three supplementary figures and one supplementary table. Two figures are presented to provide broader examples of geologic features discussed in the text. This includes regions where substantial geologic evolution was discovered or was expected but absent in the new *JunoCam* imagery (S1). It also includes a visual demonstration of the changes to geologic units that are described in Table 1 of the paper (S2).

One figure indicates where scarp height measurements were made based on shadow length (S3).

Table S1 includes measurements made of the individual block units within the blocky deposit geologic unit. Length and width measurements are geodesic and height measurements are calculated from shadow length. Longitudes are given in 0-180, East Positive regime.

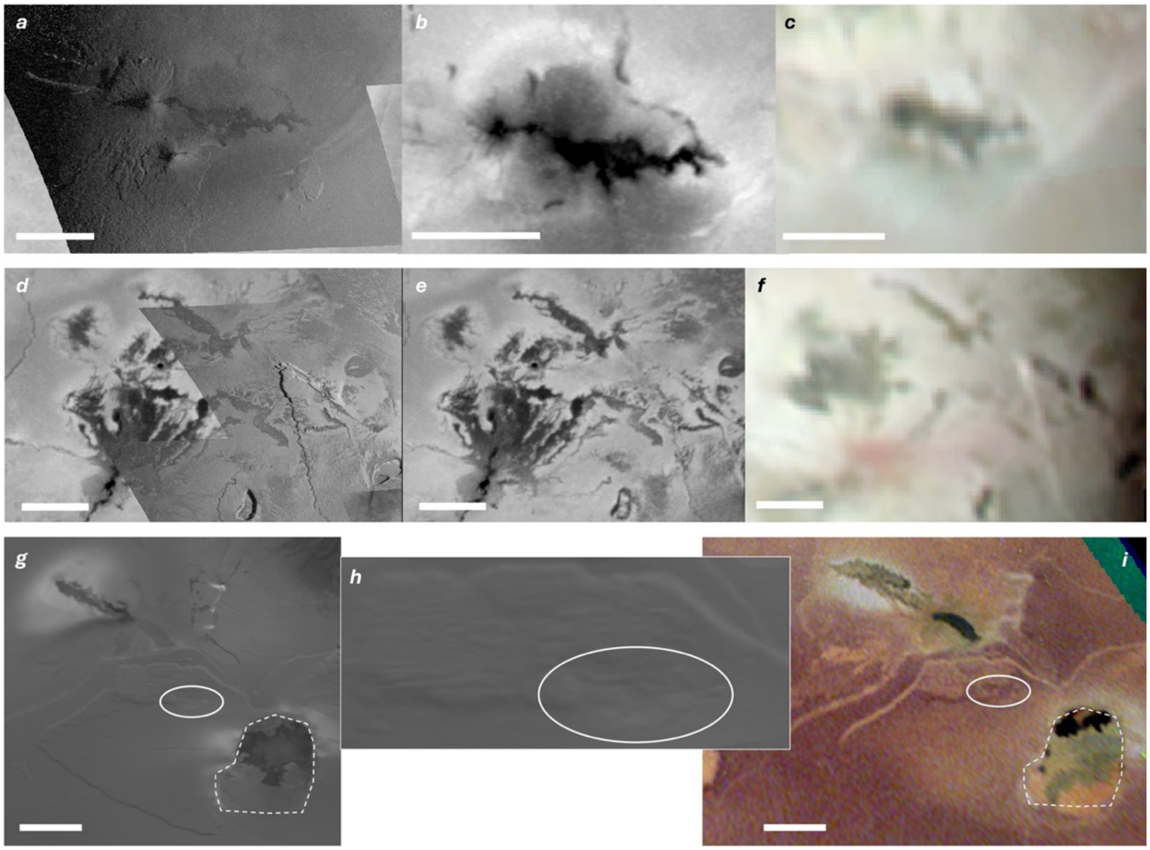

Figure S1. Summary of observations in active regions that did or did not experience measurable change between *Galileo* and JunoCam datasets. Scale bar in all images is 100 km, north is up, and projection is cylindrical. No measurable changes were seen in the Zamama volcanic flow field (18° N, 173° W) between *Galileo* high resolution (a), low resolution (b), and JunoCam (c). However, significant changes to another large flow field were observed at 32° N, 168° W, where dendritic flows fanning northward, visible in *Galileo* high resolution (d) and low resolution (e), became mantled in the southern portion by a new red diffuse deposit visible in the JunoCam image (f). Significant changes were observed in the internal structure of Creidne Patera (white dashed outline in (g) and (i); 52° S, 17° E) between *Galileo* low resolution imaging (g) and JunoCam PJ58 Jupitershine imaging (i), and some putative evolution of tectonic slumping, evidenced by the wrinkled texture on the flanks of Euboea Mons (h), is discernable in the JunoCam Jupitershine image (i), though at the given resolution it is difficult to be certain.

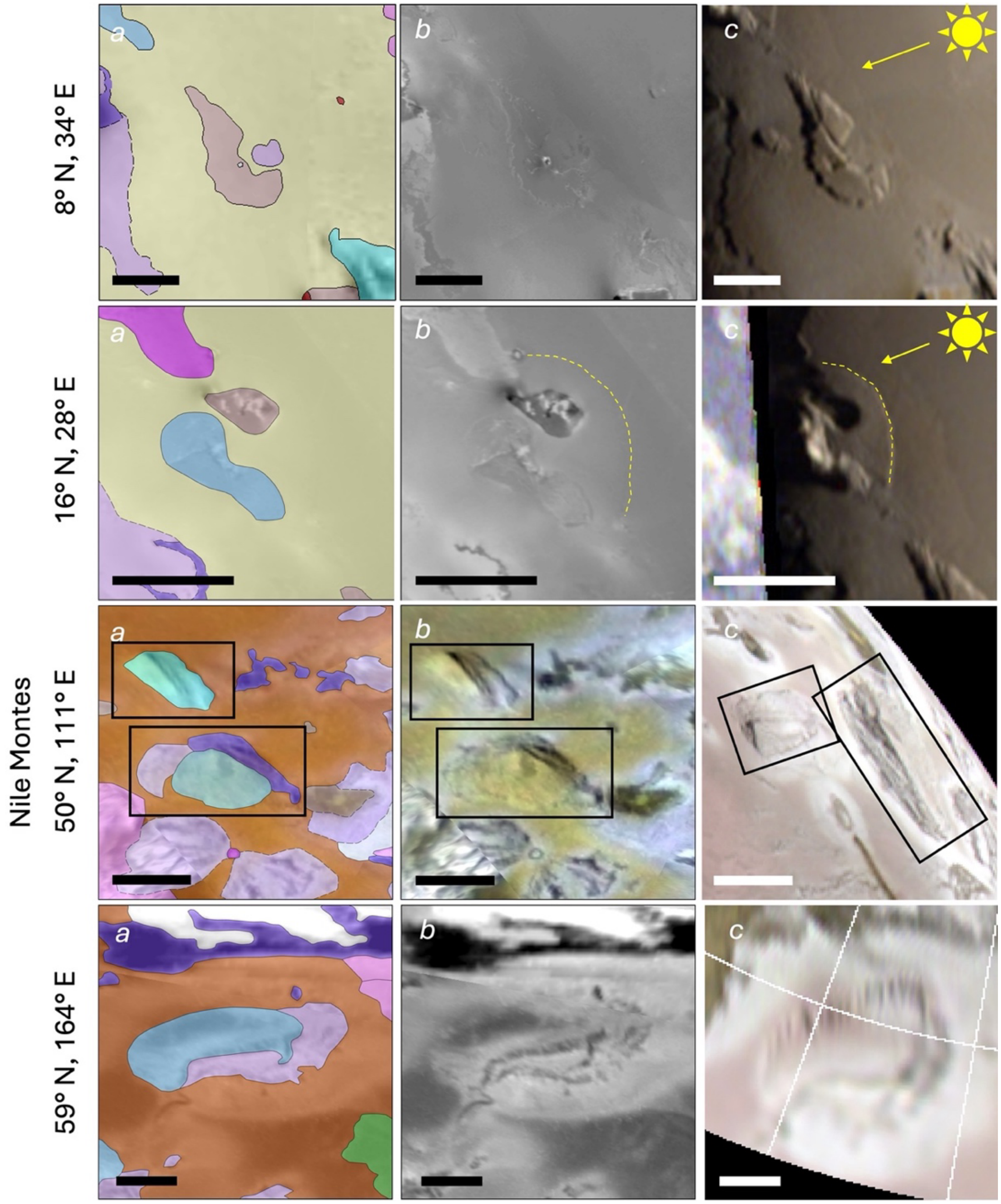
8° N, 34° E
16° N, 28° E
Nile Montes
50° N, 111° E
59° N, 164° E
a
b
c

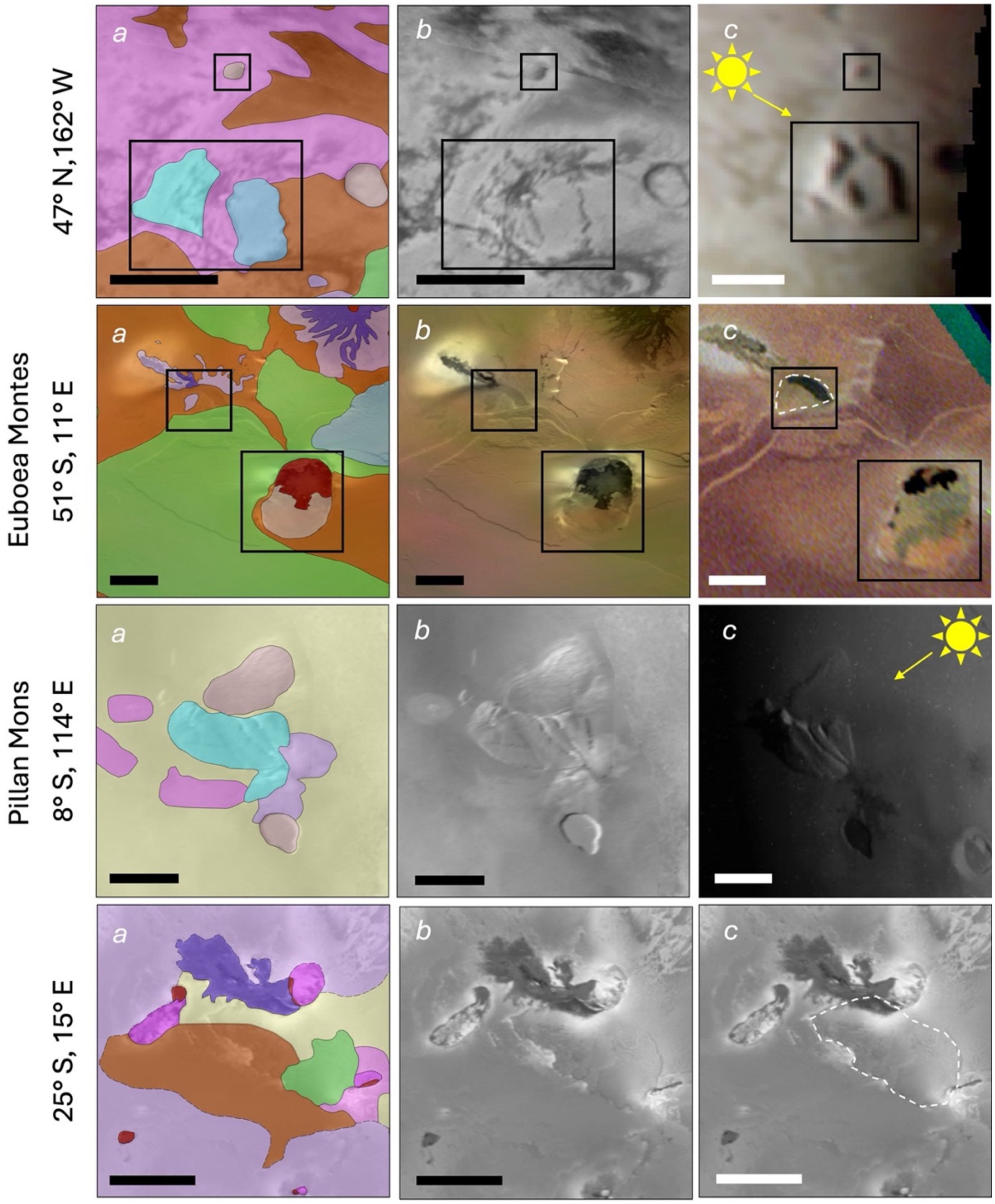

Figure S2. Reclassified geologic units based on JunoCam imagery, as outlined in Table 1. Each row represents a different region, where column *a* includes previous mapping (Williams et al., 2011), column *b* is the *Galileo* and *Voyager* basemap that mapping was based on, and column *c* is the new perspective given by JunoCam (or, in the last two examples, by other *Galileo* views examined as a result of the reclassification exercise). The scale bar in all images is 100 km and north is up. Image centers and feature names (where applicable) are given for each row.

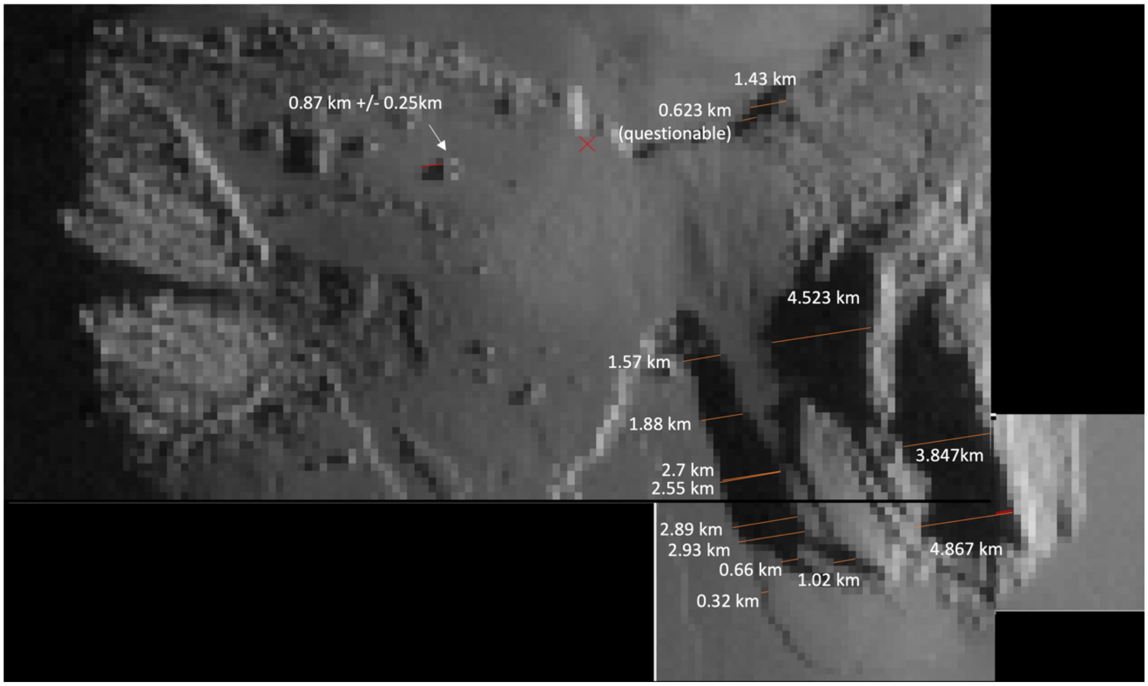

Figure S3. Height measurements of layered plains and East Cocytus Mons as calculated from shadow measurements made following solar azimuth angle across the surface at each location.

Table S1. Measured parameters for individual blocks within blocky deposit geologic unit. Blocks with height of 0 did not have sufficient shadow for measurement.

OBJECTID	Latitude	Longitude	Distance_from_summit_km	Shadow_Length_km	Sun_Azimuth	Block_Height_km	Block_Length_km	Block_Width_km	Length/Height	Block_Volume	Height/Width	Notes
2	60.82736	27.22542	91.78831	3.98967	171.205	0.61727704	25	10.31	0.02469108	159.103158	0.05987168	
3	61.34847	29.08219	117.8498	5.89295	171.256	0.90638004	7.963458	6.109391	0.11381739	44.0970916	0.14835849	
4	61.40018	29.91731	130.1045	1.9787	171.282	0.30341986	4.310261	3.681861	0.07039478	4.81520701	0.08240937	
5	61.71269	29.43829	119.5433	2.05026	171.322	0.31292824	4.553362	3.991073	0.06872466	5.68678231	0.07840704	
6	61.55223	28.3228	106.2353	4.03742	171.283	0.61903811	4.088776	3.097008	0.15139937	7.83886223	0.19988263	
7	61.79947	28.35242	102.8229	7.851	171.313	1.19954884	6.018405	5.354456	0.19931341	38.6558029	0.22402814	
8	62.44519	28.4458	98.72833	1.96581	171.415	0.29677441	5.30384	4.298704	0.05595463	6.76634923	0.06903811	
9	62.51799	27.73345	89.10432	2.399	171.41	0.36238637	3.964229	3.699314	0.09141409	5.31436995	0.09796042	
10	62.64931	27.68081	88.35094	4.05895	171.42	0.6124093	3.573106	3.182543	0.1713941	6.96405126	0.19242766	Questionable
11	62.77937	27.98107	92.40863	2.25284	171.455	0.3384983	3.911666	3.111817	0.08653558	4.12033294	0.10877835	Might be connected to 12
12	62.90679	27.69647	87.21747	4.05944	171.456	0.6098748	6.288322	5.3635	0.0969853	20.5695003	0.11370836	Might be connected to 11
14	63.32523	28.14186	94.41869	5.98567	171.515	0.89296239	8.113219	5.030621	0.11006265	36.4458402	0.1775054	
15	62.77551	28.57093	100.5964	2.06096	171.464	0.30933652	3.933472	3.702616	0.07864211	4.5052193	0.0835454	
16	63.03143	27.36022	82.67974	6.15437	171.466	0.92351074	3.769524	2.609415	0.24499399	9.08388479	0.35391486	
17	63.04311	26.79482	75.26822	6.12427	171.453	0.92041489	2.85502	2.60837	0.32238474	6.85428232	0.35286976	
18	63.13462	25.67455	58.51562	4.25178	171.426	0.64104788	5.228058	3.542861	0.12261683	11.8736701	0.18094074	
19	63.32553	26.338	69.94021	2.38752	171.471	0.35805277	3.869124	2.66742	0.09254104	3.69531183	0.13423187	
22	63.77364	27.51257	88.63478	5.99468	171.565	0.88895946	7.751596	5.094634	0.11468083	35.106382	0.17448937	
23	63.61807	26.65381	75.28506	6.1841	171.504	0.92377857	6.084951	5.099716	0.15181364	28.6662549	0.18114314	
24	63.47401	25.70115	60.26467	7.72544	171.46	1.16008916	7.476936	6.626255	0.15515569	57.4755554	0.17507463	Might be combined with 25
25	63.67261	25.85457	65.1756	6.06259	171.483	0.90789921	7.542783	6.969955	0.12036661	47.7308564	0.13025898	Might be combined with 24
27	63.87855	25.74367	66.88969			0	4.597477	3.971221	0	0	0	Can't see shadow, might be part of 24/25
28	63.895	26.30843	74.23896	4.11979	171.536	0.61306063	4.149945	3.486604	0.14772741	8.87050599	0.17583317	
29	64.02178	27.00985	85.65938	2.02886	171.583	0.30021111	2.82476	2.687983	0.10627845	2.27947498	0.11168639	
30	63.77296	29.5466	116.8811	4.00741	171.645	0.58854715	4.49497546	4.287637	0.13093445	11.3429652	0.13726609	
31	63.70176	24.88313	52.63183	8.09334	171.451	1.21663479	7.959268	3.807342	0.15285762	36.8684812	0.31954965	
32	63.70427	24.01612	44.03091	2.10627	171.432	0.31734022	3.785891	2.022348	0.08382181	2.42968021	0.15691672	
33	63.98037	24.11581	48.79938	3.9535	171.45	0.59438213	9.397274	4.852911	0.06325049	27.1062827	0.1224795	Uncertain about shadow shape
34	64.09924	25.04491	63.08957	4.11669	171.508	0.61465582	6.303148	5.337621	0.09751569	20.6793667	0.11515539	
35	64.07764	23.49324	47.33109			0	3.942632	3.910132	0	0	0	Can't see shadow
36	63.11675	24.99944	49.68889	3.97648	171.403	0.60117309	5.753286	3.571932	0.10449213	12.3543152	0.16830474	
37	61.73606	26.57073	79.83421	5.92367	171.286	0.90793026	5.942057	4.63493	0.1527973	25.0053239	0.19588867	
38	62.07546	27.48255	89.38851			0	3.961482	2.084171	0	0	0	Can't see shadow
39	62.04813	27.21843	82.41064	4.04491	171.345	0.61570735	22.470319	6.250268	0.02740092	86.4733357	0.09850895	Sinuous
40	62.26382	26.24914	67.91234	11.5847	171.349	1.76257018	14.69674	10.38188	0.11992933	268.932589	0.1697737	High uncertainty on shadow shape
41	62.26467	26.80796	77.7942	1.95438	171.356	0.29710755	4.007376	2.609314	0.07414017	3.10670576	0.11386424	High uncertainty, hard to see shadow
42	62.02707	26.64276	77.16136			0	5.350193	3.904117	0	0	0	Can't see shadow
43	61.69993	26.00226	72.79575	4.14899	171.28	0.63636695	4.187555	4.163275	0.15196623	11.0943851	0.15285249	High uncertainty
44	61.01479	25.69715	82.01346	5.92702	171.204	0.91712748	4.39102094	4.043665	0.20886429	16.2843483	0.226806	
45	60.95207	25.14128	78.31122	3.93392	171.2	0.60900299	3.57205982	2.178739	0.1704907	4.73961819	0.27952086	
48	63.11281	29.37173	112.7948	3.99783	171.539	0.59469796	2.71908349	2.314218	0.21871265	3.74216782	0.25697577	